

1 **Abrupt excursions in water vapor isotopic variability at the Pointe
2 Benedicte observatory on Amsterdam Island**

3
4 Amaëlle Landais^{1,*}, Cécile Agosta^{1,*}, Françoise Vimeux^{1,2}, Olivier Magand³, Cyrielle Solis¹,
5 Alexandre Cauquoin⁴, Niels Dutrievoz¹, Camille Risi⁵, Christophe Leroy-Dos Santos¹, Elise
6 Fourré¹, Olivier Cattani¹, Olivier Jossoud¹, Bénédicte Minster¹, Frédéric Prié¹, Mathieu
7 Casado¹, Aurélien Dommergue⁶, Yann Bertrand⁶, Martin Werner⁷

8
9 ¹ Laboratoire des Sciences du Climat et de l'Environnement, LSCE/IPSL, CEA-CNRS-UVSQ,
10 Université Paris-Saclay, 91191 Gif-sur-Yvette, France

11 ² HydroSciences Montpellier (HSM), UMR 5569 (UM, CNRS, IRD), 34095 Montpellier, France

12 ³ Observatoire des Sciences de l'Univers de La Réunion (OSU-Réunion), UAR 3365,
13 Université de La Réunion, CNRS, IRD, Météo France, Saint-Denis, La Réunion, France

14 ⁴ Institute of Industrial Science (IIS), The University of Tokyo, Kashiwa, Japan.

15 ⁵ Laboratoire de Météorologie Dynamique, Institut Pierre - Simon Laplace, Sorbonne Université /
16 CNRS / École Polytechnique – IPP, Paris, France

17 ⁶ Univ. Grenoble Alpes, CNRS, INRAE, IRD, Grenoble INP^T, IGE, 38000 Grenoble, France
18 (^TInstitute of Engineering and Management Univ. Grenoble Alpes)

19 ⁷ Alfred Wegener Institute, Helmholtz Centre for Marine and Polar Research, D-27570 Bremerhaven,
20 Germany

21 * corresponding authors who contributed equally to the study: amaelle.landais@lsce.ipsl.fr and
22 cecile.agosta@lsce.ipsl.fr

23
24
25
26
27
28
29
30

31 **Abstract**

32 In order to complement the picture of the atmospheric water cycle in the Southern Ocean, we
33 have continuously monitored water vapor isotopes since January 2020 on Amsterdam Island in
34 the Indian Ocean. We present here the first 2-year-long water vapor isotopic record on this site.
35 We show that the water vapor isotopic composition largely follows the water vapor mixing
36 ratio, as expected in marine boundary layers. However, we detect 11 periods of a few days
37 where there is a strong loss of correlation between water vapor $\delta^{18}\text{O}$ and water vapor mixing
38 ratio as well as abrupt negative excursions of water vapor $\delta^{18}\text{O}$. These excursions often occur
39 toward the end of precipitation events. Six of these events show a decrease in gaseous elemental
40 mercury suggesting subsidence of air from higher altitude.

41 Our study aims at further exploring the mechanism driving these negative excursions in water
42 vapor $\delta^{18}\text{O}$. We used two different models to provide a data-model comparison over this 2-year
43 period. While the European Centre Hamburg model (ECHAM6-wiso) at 0.9° was able to
44 reproduce most of the sharp negative water vapor $\delta^{18}\text{O}$ excursions hence validating the physics
45 process and isotopic implementation in this model, the Laboratoire de Météorologie
46 Dynamique Zoom model (LMDZ-iso) at 2° (3°) resolution was only able to reproduce 7 (1) of
47 the negative excursions highlighting the possible influence of the model resolution for the study
48 of such abrupt isotopic events. Based on our detailed model-data comparison, we conclude that
49 the most plausible explanations for such isotopic excursions are rain-vapor interactions
50 associated with subsidence at the rear of a precipitation event.

52 **1. Introduction**

53 The main sources of uncertainty in the atmospheric components of Earth System Models for
54 future climate projections are associated with complex atmospheric processes, particularly
55 those related to water vapor and clouds (Arias et al., 2021; Sherwood et al., 2014). Decreasing
56 these uncertainties is of vital interest as the hydrological cycle is a fundamental element of the
57 climate system because it allows, via the transport of water vapor, to ensure the Earth's thermal
58 balance.

59 Stable water isotopes are a useful tool to study the influence of dynamical processes on the
60 water budget at various spatial and temporal scales. They provide a framework for analyzing
61 moist processes over a range of time scales from large-scale moisture transport to cloud
62 formation, precipitation, and small-scale turbulent mixing (Bailey et al., 2023; Dahinden et al.,
63 2021; Galewsky et al., 2016; Thurnherr et al., 2020).

64 The relative abundance of heavy and light isotopes in different water reservoirs is altered during
65 phase change processes due to isotopic fractionation (caused by a difference in saturation vapor
66 pressure and molecular diffusivity in the air and the ice). Each time a phase change occurs, the
67 relative abundance of water vapor isotopes is altered. We express the abundance of the heavy
68 isotopes D and ^{18}O with respect to the amount of light isotopes H and ^{16}O , respectively, in the
69 water molecules through the notation δ :

70
$$\delta^{18}\text{O} = \left(\frac{(^{18}\text{O}/^{16}\text{O})_{\text{Sample}}}{(^{18}\text{O}/^{16}\text{O})_{\text{VSMOW}}} - 1 \right) \times 1000 \quad (\text{Eq. 1})$$

71
72
$$\delta D = \left(\frac{(D/H)_{\text{Sample}}}{(D/H)_{\text{VSMOW}}} - 1 \right) \times 1000 \quad (\text{Eq. 2})$$

73
74 where $(^{18}\text{O}/^{16}\text{O})$ and (D/H) represent the isotopic ratios of oxygen and hydrogen atoms in water
75 and VSMOW (Vienna Standard Mean Ocean Water) is an international reference standard for
76 water isotopes.

77 There are two types of isotopic fractionation: equilibrium fractionation, which is caused by the
78 difference in saturation vapor pressure of different isotopes, and non-equilibrium fractionation,
79 which occurs due to molecular diffusion (e.g. during ocean evaporation in undersaturated
80 atmosphere or snowflakes condensation in oversaturated atmosphere). In the water vapor above
81 the ocean, the proportion of non-equilibrium fractionation, and hence diffusive processes can

82 be estimated by the deuterium excess, a second order isotopic variable denoted d-excess,
83 defined as (Dansgaard, 1964):

84

85
$$d\text{-excess} = \delta D - 8 \times \delta^{18}\text{O} \quad (\text{Eq.3})$$

86

87 Over the recent years and thanks to the development of optical spectroscopy enabling
88 continuous measurements of water isotopes ratios in water vapor, an increasing number of
89 studies have focused on the use of water vapor stable isotopes to document the dynamics of the
90 water cycle over synoptic weather events, such as cyclones, cold fronts, atmospheric rivers
91 (Aemisegger et al., 2015; Ansari et al., 2020; Bhattacharya et al., 2022; Dütsch et al., 2016;
92 Graf et al., 2019; Lee et al., 2019; Munksgaard et al., 2015; Tremoy et al., 2014) or water cycle
93 processes such as evaporation over the ocean or deep convection (Benetti et al., 2015; Bonne
94 et al., 2019). Several instruments have been installed either in observatory stations (e.g.
95 Aemisegger et al., 2012; Guilpart et al., 2017; Leroy-Dos Santos et al., 2020; Steen-Larsen et
96 al., 2013; Tremoy et al., 2012), on boat (e.g. Benetti et al., 2014; Thurnherr et al., 2019) or on
97 aircraft (Henze et al., 2022). In the aforementioned studies, the interpretation of the isotopic
98 records is often performed using a hierarchy of isotopic models, from conceptual models
99 (Rayleigh type) to general circulation models or regional weather prediction models equipped
100 with water isotopes (Ciais and Jouzel, 1994; Markle and Steig, 2022; Risi et al., 2010; Werner
101 et al., 2011). Such data comparisons enable one to test the performances of the models either in
102 the simulation of the dynamic of the atmospheric water cycle or in the implementation of the
103 water isotopes. Our study is part of these dynamics analyses and aims at improving the
104 documentation of climate and atmospheric water cycle in the Southern Indian Ocean, a region
105 which has been poorly documented until now.

106 Over the previous years, we have installed three water vapor analyzers on La Reunion Island at
107 the Maïdo observatory, 21.079°S, 55.383°E, 2160m (Guilpart et al., 2017) and in Antarctica
108 (Dumont d'Urville, 66.663°S, 140°E, 202m and Concordia, 75.1°S, 123.333°E, 3233m; Bréant
109 et al., 2019; Casado et al., 2016; Leroy-Dos Santos et al., 2021). These instruments have been
110 used for the following purposes. They document the diurnal variability of the isotopic signal
111 with the influence of the subtropical westerly jet on the water isotopic signal in night as well as
112 the cyclonic activity on La Réunion Island. In Antarctica, the records have shown a strong
113 influence of katabatic winds on the isotopic composition of water vapor (Bréant et al., 2019).
114 In order to complete the picture of the atmospheric water cycle over the Indian basin of the
115 Southern Ocean already measured by these three analyzers, we installed a new water vapor

116 isotopic analyzer at mid-latitude in the south Indian Ocean on Amsterdam Island (Figure 1) in
117 November 2019. Amsterdam Island is one of the very rare atmospheric observatories in the
118 southern hemisphere. Moreover, the south Indian Ocean is a significant moisture source for
119 Antarctic precipitation, notably in the region encompassing Dumont d'Urville and Concordia
120 stations (Jullien et al., 2020; Wang et al., 2020).

121 The objective of this study is to provide the first analyses of isotopic records (vapor and
122 precipitation) on Amsterdam Island, with a comparison of meteorological data and
123 environmental data collected in parallel on the Amsterdam Island Observatory (e.g.
124 atmospheric mercury) to help with the interpretation of isotopic records. Indeed, previous
125 studies have shown that gaseous elemental mercury decreases with increasing altitude in marine
126 environment suggesting that gaseous elemental mercury can be used as a tracer of subsidence
127 of air from the high altitude (e.g. Koenig et al., 2023). This study includes analyses of
128 meteorological maps, back trajectories as well as outputs from general circulation models
129 equipped with water isotopes. After a description of the different records over the years 2020
130 and 2021, model simulations and back trajectories, we focus on some low-pressure events
131 associated with a strong negative excursion of $\delta^{18}\text{O}_v$ over a few days and a decoupling between
132 $\delta^{18}\text{O}_v$ and humidity. These events are then used for evaluation of atmospheric component of
133 Earth system models equipped with water isotopes.

134

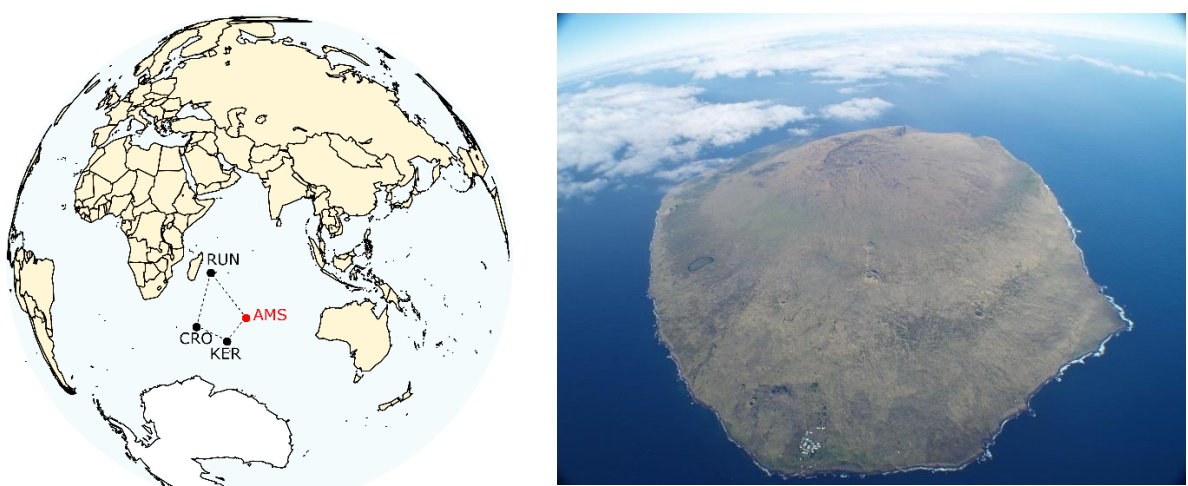
135 **2. Methods**

136 **2.1 Site**

137 Labelled as a global site for the Global Atmosphere Watch World Meteorological Organization,
138 Amsterdam Island (37.7983°S , 77.5378°E) is a remote and very small island of 55 km^2 with
139 a population of about 30 residents, located in the southern Indian Ocean at 3300 km and 4200 km
140 downwind from the nearest lands, Madagascar, and South Africa, respectively (Sprovieri
141 et al., 2016). Climate is temperate, generally mild with frequent presence of clouds (average
142 total sunshine hours is 1581 hours per year over the period 1981 – 2010 from MeteoFrance
143 data). Seasonal boundaries are defined as follows: winter from July to September and summer
144 from December to February, in line with previous studies (Sciare et al., 2009). Average
145 temperature is lower in winter compared to summer (10.5°C vs 15°C) while relative humidity
146 and wind speed remain high (50-85% and 5 to 15 m s^{-1} respectively) most of the year without
147 a clear seasonal cycle.

148 Numerous atmospheric compounds and meteorological parameters are and were continuously
149 monitored at the site since 1960 (Angot et al., 2014; El Yazidi et al., 2018; Gaudry et al., 1983;
150 Gros et al., 1999, 1998; Polian et al., 1986; Sciare et al., 2000, 2009; Slemr et al., 2015; Slemr
151 et al., 2020). In particular, the Amsterdam (AMS) site hosts several dedicated atmospheric
152 observation instruments notably at the Pointe Bénédicte atmospheric observatory (70 m above
153 sea level) where greenhouse gases concentrations and mercury (Hg) are monitored. Hg species
154 have been continuously measured since 2012.

155



156
157
158 **Figure 1** : Location (left) and picture (right) of Amsterdam Island. CRO: Crozet Island;
159 RUN: La Réunion Island; KER: Kerguelen Island; AMS: Amsterdam Island.
160 Picture credit: left – from O. Magand adapted from Angot et al. (2016); right – photo
161 taken by O. Magand.

162

163 **2.2 Long term measurements**

164 2.2.1 Meteorological measurements

165

166 One meteorological station is installed at the top of an observation mast (25 m above ground
167 level, hence 95 m above sea level) at the Pointe Bénédicte observatory since 1980 (data used
168 during this study). Wind speed and direction, atmospheric pressure, air temperature and relative
169 humidity data are currently obtained at a minute resolution. Another meteorological station is
170 based on the island and is operated by Météo France at Martin-de-Viviès life base around 27 m

171 above sea level, about two kilometers east from the Pointe Bénédicte observatory collecting air
172 temperature, humidity, precipitation, wind speed and direction, pressure and solar radiation
173

174 2.2.2 Gaseous elemental mercury (GEM)

175

176 Atmospheric GEM (Gaseous Elemental Mercury) measurements have been conducted since
177 2012 in the framework of IPEV GMOSTral-1028 observatory program at the Pointe Benedicte
178 atmospheric research facility (Magand and Dommergue, 2022). GEM is continuously measured
179 (15-minute data frequency acquisition) using a Tekran 2537 A/B instrument model (Angot et
180 al., 2014; Li et al., 2023; Slemr et al., 2015, 2020; Sprovieri et al., 2016). The measurement is
181 based on mercury enrichment on a gold cartridge, followed by thermal desorption and detection
182 by cold vapor atomic fluorescence spectroscopy (Bloom and Fitzgerald, 1988; Fitzgerald and
183 Gill, 1979). Concentrations are expressed in nanograms per cubic meters at standard
184 temperature and pressure conditions (273.15 K and 1013.25 hPa) with an instrumental detection
185 limit below 0.1 ng m⁻³ and a GEM average uncertainty value around 10% (Slemr et al., 2015).
186 The instrument is automatically calibrated following a strict procedure adapted from that of
187 Dumarey et al. (1985). Ambient air is sampled at 1.2 L min⁻¹ through a heated (50°C) and UV
188 protected PTFE sampling line, with an inlet installed outside, 6 m above ground level (76 m
189 above sea level). The air is filtered through two 0.45 µm pore size polyether sulphone and one
190 PTFE (polytetrafluoroethylene) 47 mm diameter filters before entering in Tekran to prevent the
191 introduction of any particulate material into the detection system as well as to capture any
192 gaseous oxidized mercury or particulate bound mercury species ensuring that only GEM is
193 sampled. To ensure the comparability of mercury measurements around the world, the
194 instrument is operated according to the Global Mercury Observation System standard operating
195 procedures (Sprovieri et al., 2016; Steffen et al., 2012).

196 In this study, and even though long-range transport and a variable tropopause height may
197 modulate the signal, atmospheric GEM is used as potential tracer of stratosphere-to-troposphere
198 intrusion and/or subsidence of upper troposphere air (above 5-6 km) that may impact the

199 atmospheric records at the Pointe Benedicte Observatory where marine boundary layer air is
200 collected most of the time (Angot et al., 2014; Slmer et al., 2015, 2020; Sprovieri et al., 2016).

201 Mercury in the atmosphere consists of three forms: gaseous elemental mercury (GEM as
202 defined above), gaseous oxidized mercury and particulate-bound mercury. GEM, the dominant
203 form of atmospheric mercury, is ubiquitous in the atmospheric reservoir and originates from a
204 multitude of anthropogenic and natural sources (Edwards et al., 2021; Gaffney et al., 2014;

205 Gustin et al., 2020 ; Gworek et al., 2020). Near the surface (marine or terrestrial boundary layer)
206 and out of polar regions, gaseous oxidized mercury and particulate-bound mercury represent
207 only a few percent of the total atmospheric mercury (Gustin and Jaffe, 2010; Gustin et al., 2015;
208 Swartzendruber et al., 2006). Chemical cycling and spatiotemporal distribution of mercury in
209 the air is still poorly understood whatever atmospheric layer considered (surface, mixed or free
210 troposphere, stratosphere), and complete GEM oxidation schemes remain unclear (Shah et al.,
211 2021 and associated references). Still, several studies provided evidence that vertical
212 distribution of atmospheric mercury measurements from boundary layer to lower/upper
213 troposphere and stratosphere shows a decreasing trend in GEM concentration with increasing
214 altitude, in parallel with an increase in the concentration of divalent mercury resulting from
215 GEM oxidation mechanisms (Brooks et al., 2014; Fain et al., 2009; Fu et al., 2016; Koenig et
216 al., 2023; Lyman and Jaffe, 2012; Murphy et al., 2006; Swartzendruber et al., 2006, 2008; Sheu
217 et al., 2010; Talbot et al., 2007). The identification of such observational processes (lower
218 concentration of GEM in high-altitude air masses compared to those in the marine boundary
219 layer ones) is used here to help characterize possible intrusions of high-altitude air masses at
220 the low altitude Pointe Benedicte observatory.

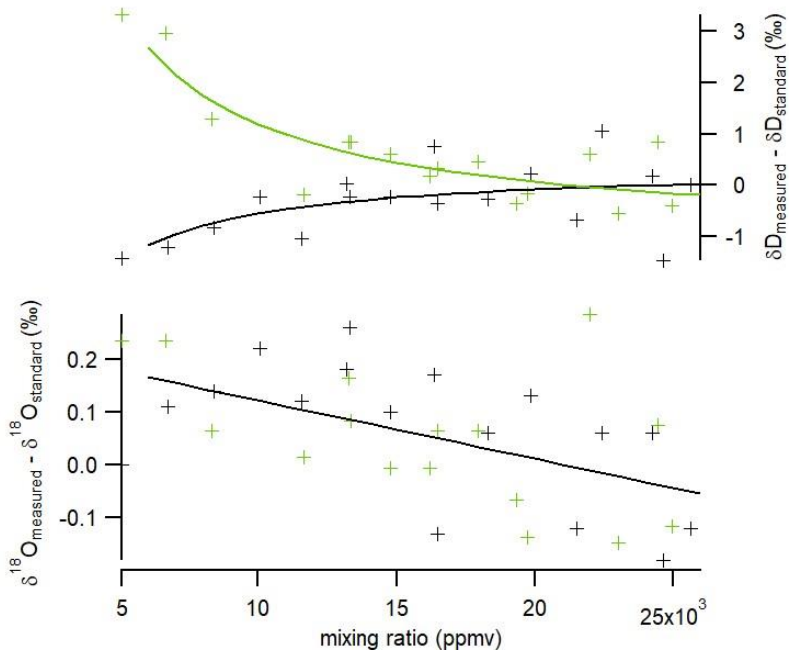
221

222 **2.3 Water vapor isotopic measurements**

223

224 The near-surface water vapor $\delta^{18}\text{O}$ and δD (hereafter $\delta^{18}\text{O}_v$ and δD_v expressed in ‰ versus
225 SMOW and enabling to calculate water vapor d-excess_v as d-excess_v = $\delta\text{D}_v - 8 \times \delta^{18}\text{O}_v$). The
226 water vapor mixing ratio (q_v in ppmv) have been measured continuously since November 2019.
227 The measurements have been done with a Picarro Inc. instrument (L2130-i model) based on
228 wavelength-scanned cavity ring down spectroscopy. The instrument has been installed in a
229 temperature-controlled room at the Amsterdam Island observatory and the sampling of water
230 vapor is done outside at ~ 6 m above ground level (or 76 m above sea level) through a 5 m long
231 inlet tube made of PFA (perfluoroalkoxy alkanes) and heated at 40°C.

232



233

234 **Figure 2:** Influence of the water vapor mixing ratio on measured δD (top) and $\delta^{18}\text{O}$ (bottom)
 235 (anomaly from the true value of the standard). The results are shown for two different
 236 standards (GREEN_AMS in green and EPB_AMS in black). The crosses indicate the data
 237 obtained with the set-up and the solid lines are the best regression curves (same curve for
 238 $\delta^{18}\text{O}$ for both standards).

239

240 The calibration of water vapour mixing ratio was performed in the laboratory before sending
 241 the instrument to Amsterdam Island. In the field, we found an excellent agreement between
 242 mixing ratio measured by the Picarro instrument and mixing ratio measured by the weather
 243 station (the difference between the two records always stays below 2% and there is no
 244 systematic shift between the two records).

245 The calibration of the water isotopic data is performed in several steps following previous
 246 studies (Leroy-Dos Santos et al., 2020; Tremoy et al., 2011) and using a standard delivery
 247 module by Picarro. First, we quantified the influence of the water vapor mixing ratio on the
 248 water isotope ratios. This effect is large at very low humidity (Leroy-Dos Santos et al., 2021).

249 It can also depend on the isotopic composition of the standard water (Weng et al., 2020).

250 Here, we introduced two different water standards, EPB-AMS and GREEN-AMS, with
 251 respective values of (-5.66 ‰, -47.31 ‰) and (-32.65 ‰, -263.76 ‰) for the couple ($\delta^{18}\text{O}$,
 252 δD) which encompass the isotopic values observed on site. While we would expect a constant
 253 null value for ($\delta^{18}\text{O}_{\text{measured}} - \delta^{18}\text{O}_{\text{standard}}$) in Figure 2 because we always inject the same water
 254 standards, the measured $\delta^{18}\text{O}$ values of both EPB-AMS and GREEN-AMS standards in fact

255 decrease with increasing humidity with the same amplitude. The $(\delta D_{\text{measured}} - \delta D_{\text{standard}})$
 256 displayed in Figure 2 also shows variations but in contrast to the relative evolution of $\delta^{18}\text{O}$
 257 with respect to water vapor mixing ratio, the δD measurements of EPB-AMS and GREEN-
 258 AMS standards exhibit different behavior: δD of EPB-AMS increases by 1.5‰ and δD of
 259 GREEN-AMS decreases by 2.5‰ over the same 6,000-24,000 ppmv range for water vapor
 260 mixing ratio q_v .

261 As a consequence, the raw $\delta^{18}\text{O}_v$ measurements are corrected with the following regression:

262

$$263 \quad \delta^{18}\text{O}_{v,\text{corr}} = \delta^{18}\text{O}_{v,\text{measured}} + 1.1 \cdot 10^{-5} \times q + 0.232 \quad (\text{Eq 4})$$

264

265 For the correction of the raw δD_v , we use two different regression splines for EPB-AMS and
 266 GREEN-AMS (cf Figure 2):

267

$$268 \quad \delta D_{EPB-AMS,\text{corr}} = \delta D_{EPB-AMS,\text{measured}} + \frac{9300}{q} - 0.383 \quad (\text{Eq 5})$$

$$269 \quad \delta D_{GREEN-AMS,\text{corr}} = \delta D_{GREEN-AMS,\text{measured}} - \frac{22400}{q} + 1.05 \quad (\text{Eq 6})$$

270

271 The raw δD_v are thus weighted-corrected according to their distance to the EPB_AMS and the
 272 GREEN_AMS splines as follows:

273

274

$$275 \quad \delta D_{v,\text{corr}} = \delta D_{GREEN-AMS,\text{corr}} + \frac{\delta D_{v,\text{measured}} - \delta D_{GREEN-AMS,\text{measured}}}{\delta D_{EPB-AMS,\text{measured}} - \delta D_{GREEN-AMS,\text{measured}}} \times (\delta D_{EPB-AMS,\text{corr}} - \delta D_{GREEN-AMS,\text{corr}}) \\ 276 \quad (\text{Eq 7})$$

277

278 This first calibration step (correction from the influence of mixing ratio on the isotopic
 279 composition) has been performed every year over the whole range of mixing ratio values and
 280 provided very similar results from one year to the other. The second calibration step consists in
 281 the injection of the same two isotopic standards every 47 h at a water vapor mixing ratio of
 282 13,000 ppmv to correct for any long-term drift. The correction associated with this drift is less
 283 than 0.4‰ for $\delta^{18}\text{O}$ and 2.5‰ for δD over the two years of measurements.

284 Precipitation were also sampled on a weekly basis in a rain gauge filled with paraffin oil which
285 permits to have measurements of water isotopic composition in the precipitation on a weekly
286 basis. The water samples are then sent for analyses to LSCE (Laboratoire des Sciences du
287 Climat et de l'Environnement) and measured with an isotopic analyzer L2130-i by Picarro. The
288 uncertainty associated with this series of measurements is of $\pm 0.15 \text{ ‰}$ for $\delta^{18}\text{O}$ and $\pm 0.7 \text{ ‰}$ for
289 δD leading to an uncertainty of $\pm 1.4 \text{ ‰}$ for d-excess.

290

291 **2.4 Back trajectories: FLEXPART**

292
293 The origin and trajectory of air masses were calculated by FLEXPART, which is a Lagrangian
294 particle dispersion model (Pisso et al., 2019). All the meteorological data used to simulate the
295 back trajectories are taken from the ERA5 atmospheric reanalysis (Hersbach et al., 2020) with
296 a 6-hourly resolution. The ERA5 reanalysis is carried out by the European Center for Medium-
297 Range Weather Forecasts (ECMWF), using ECMWF's Earth System model IFS (Integrated
298 Forecasting System), cycle 41r2. For a few selected events, we used FLEXPART to calculate
299 back trajectories over 5 days with 1000 launches of neutral particles (sensitivity test) of inert
300 air tracers released randomly (volume of $0.1^\circ \times 0.1^\circ \times 100 \text{ m}$) every 3 hours at 100 m above sea
301 level (Leroy-Dos Santos et al., 2020) centered around the coordinates of Amsterdam Island.
302 The results of the FLEXPART back trajectories are then displayed as particle probability
303 density as well as through the location of their humidity weighted averages.

304 **2.5 General atmospheric circulation model equipped with water stable 305 isotopes**

306

307 **2.5.1 LMDZ-iso model (Laboratoire de Météorologie Dynamique Zoom model 308 equipped with water isotopes)**

309
310 LMDZ-iso (Risi et al., 2010) is the isotopic version of the atmospheric general circulation
311 model LMDZ6 (Hourdin et al., 2020). We have used LMDZ-iso version 20230111.trunk with
312 the physical package NPv6.1, identical to the atmospheric setup of IPSL-CM6A (Boucher et
313 al., 2020) used for phase 6 of the Coupled Model Intercomparison Project (CMIP6, Eyring et
314 al., 2016). We performed two simulations, one at very low horizontal resolution (VLR, 3.75°
315 in longitude and 1.9° in latitude, 96×95 grid cells) and the second at low horizontal resolution
316 (LR, 2.0° in longitude and 1.67° in latitude, 144×142 grid cells). Both simulations have 79

317 vertical levels and the first atmospheric level is located around 10 m above ground level. The
318 LMDZ-iso 3D-fields of temperature and wind are nudged toward the 6-hourly ERA5 reanalysis
319 data with a relaxation time of 3 hours. Surface ocean boundary conditions are taken from the
320 monthly mean SST and sea-ice fields from the CMIP6 AMIP Sea Surface Temperature and Sea
321 Ice dataset version 1.1.8 (Durack et al., 2022; Taylor et al., 2000). LMDZ-iso outputs are used
322 at a 3-hourly resolution. Amsterdam Island (58 km²) is too small to be represented in the
323 LMDZ-iso model.

324

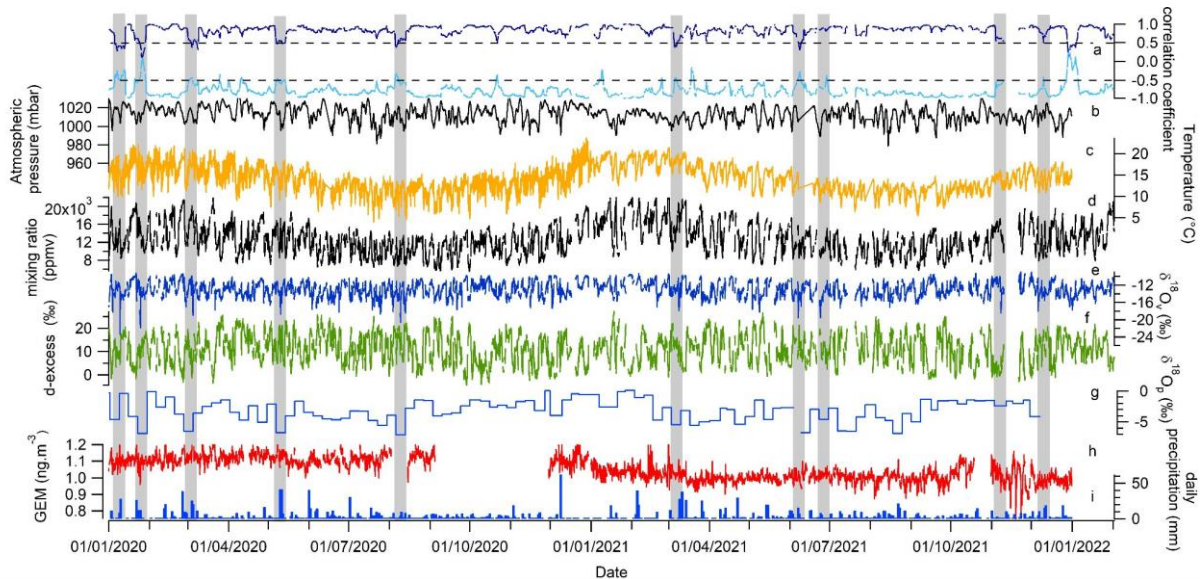
325 **2.5.2 ECHAM6-wiso model (European Centre Hamburg model equipped with water
326 isotopes)**

327

328 ECHAM6-wiso (Cauquoin et al., 2019; Cauquoin and Werner, 2021) is the isotopic version of
329 the atmospheric general circulation model ECHAM6 (Stevens et al., 2013). The
330 implementation of the water isotopes in ECHAM6 has been described in detail by Cauquoin et
331 al. (2019), and has been updated in several aspects by Cauquoin and Werner (2021) to make
332 the model results more consistent with the last findings based on water isotope observations
333 (isotopic composition of snow on sea ice considered, supersaturation equation slightly updated,
334 and kinetic fractionation factors for oceanic evaporation assumed as independent of wind
335 speed). We have used ECHAM6-wiso model outputs from a simulation with a T127L95 spatial
336 resolution (0.9° horizontal resolution and 95 vertical levels). ECHAM6-wiso is thus run with a
337 finer resolution than both LMDZ-iso simulations. The ECHAM6-wiso 3D-fields of
338 temperature, vorticity and divergence as well as the surface pressure field were nudged toward
339 the ERA5 reanalysis data every 6 hours (Hersbach et al., 2020). The orbital parameters and
340 greenhouse gas concentrations have been set to the values of the corresponding model year.
341 The monthly mean sea surface temperature and sea-ice fields from the ERA5 reanalysis have
342 been applied as ocean surface boundary conditions, as well as a mean $\delta^{18}\text{O}$ of surface seawater
343 reconstruction from the global gridded data set of LeGrande and Schmidt (2006). As no
344 equivalent data set of the δD composition of seawater exists, the δD of the seawater in any grid
345 cell has been set equal to the related $\delta^{18}\text{O}$ composition, multiplied by a factor of 8, in accordance
346 with the observed relation for meteoric water on a global scale (Craig, 1961). The ECHAM6-
347 wiso simulation is described in detail and evaluated by Cauquoin and Werner (2021).
348 ECHAM6-wiso outputs are given at a 6-hourly resolution. As for the LMDZ-iso model,
349 Amsterdam Island (58 km²) is too small to be represented by ECHAM6-wiso.

350 **3. Results**351 **3.1 Data description**

352



353 **Figure 3 :** Meteorological, isotopic and GEM records for the years 2020 and 2021 on the
 354 Amsterdam Island : (a) correlation coefficient between $\delta^{18}\text{O}_v$ and mixing ratio (dark blue, top)
 355 and between $\delta^{18}\text{O}_v$ and d-excess $_{\text{v}}$ (light blue, bottom) over a moving time window of 8 days,
 356 (b) atmospheric pressure (hourly average), (c) atmospheric temperature (hourly average), (d)
 357 water vapor mixing ratio (hourly average), (e) $\delta^{18}\text{O}_v$ (hourly average), (f) d-excess $_{\text{v}}$ (hourly
 358 average), (g) $\delta^{18}\text{O}$ of precipitation sampled on a weekly basis, (h) GEM concentration (hourly
 359 average), (i) daily precipitation. The grey shaded areas indicate the negative excursions in $\delta^{18}\text{O}_v$
 360 associated with decorrelation between water vapor mixing ratio and $\delta^{18}\text{O}_v$ and a correlation
 361 coefficient >-0.5 between d-excess $_{\text{v}}$ and $\delta^{18}\text{O}_v$.
 362

363 **3.1.1 Temporal variability in the meteorological records**

364 As mentioned earlier, there is a clear annual cycle at Amsterdam Island as recorded in the
365 temperature and water vapor mixing ratio for the years 2020 and 2021. The December-February
366 period (austral summer) has the highest temperatures with an average of 15.0°C, while in winter
367 (July-September) the average temperature varies around 10.5°C. In parallel, we do not see clear
368 patterns of a diurnal cycle in the temperature record except for some periods yet with a small
369 amplitude (4-5 °C).

370 The impact of synoptic events at the scale of a few days is visible in the temperature and water
371 mixing ratio with a covariation of temperature and water vapor mixing ratio and amplitudes of
372 up to 10°C and more than 10,000 ppmv.

373

374 **3.1.2 Temporal variability in the GEM record**

375 Previous studies clearly showed that AMS is little influenced by anthropogenic sources of
376 mercury, and greatly influenced by the ocean surrounding the island (Angot et al., 2014; Hoang
377 et al., 2023; Jiskra et al., 2018; Li et al., 2023; Slemr et al., 2015, 2020). Angot et al., 2014
378 reported mean annual GEM concentrations of about $1.03 \pm 0.08 \text{ ng m}^{-3}$ from 2012 to 2013.
379 These concentrations are ~30% lower than those measured at remote sites of the northern
380 hemisphere. Over the period 2012 to 2017, Slemr et al. (2020) confirmed that higher GEM
381 concentrations can be found during austral winter. Lower GEM values are generally observed
382 in October and November, as well as in January and February during austral summer. Using
383 this 6-year long data set, mean annual GEM concentration is $1.04 \pm 0.07 \text{ ng m}^{-3}$ (annual range:
384 1.014 to 1.080 ng m^{-3}) i.e. very close to the one observed by Angot et al. (2014).

385 Surprisingly, unlike the 2012-2017 data set, GEM presented in this study did not show a
386 significant higher mean concentration during the austral winter months than during the summer
387 months (Figure 3), with consequently no discernible seasonal amplitude of GEM. On a finer
388 timescale, the lack of a clear pattern of GEM seasonal cycle is counterbalanced by days showing
389 abrupt increases or decreases in concentrations. Some of the sudden GEM decreases appear
390 concomitant with important negative peaks of several ‰ in $\delta^{18}\text{O}_v$.

391

392 **3.1.3 Temporal variability of water isotopic composition**

393 The isotopic composition of precipitation ($\delta^{18}\text{O}_p$) sampled on a weekly basis displays a quite
394 large variability ($\delta^{18}\text{O}_p = -3.06 \pm 1.75 \text{ ‰}$, $n=104$) with values slightly higher during austral
395 summer (difference between summer and winter $\delta^{18}\text{O}_p$ values is about 2 to 3 ‰) (Figure 3). No

396 significant seasonal variations are observed in the record of d-excess of precipitation (not
397 shown).

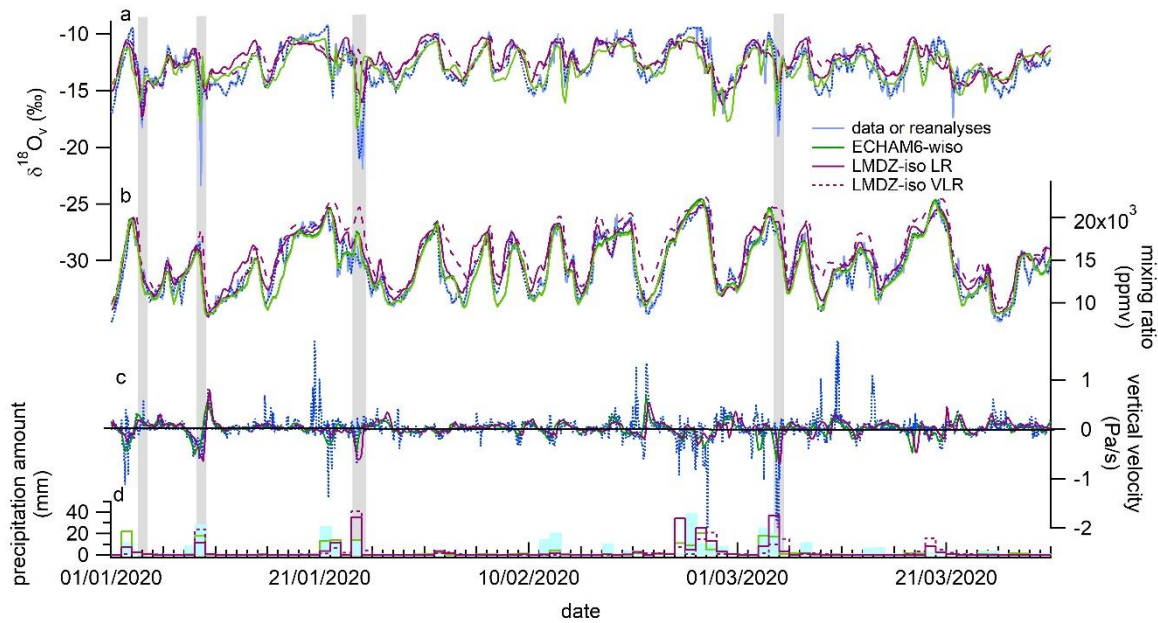
398 No diurnal cycle can be detected in the $\delta^{18}\text{O}_v$ and d-excess_v. An annual cycle is not visible either
399 (1 ‰ difference between summer and winter mean $\delta^{18}\text{O}_v$ value while standard deviation of the
400 entire record at 1 h resolution is 1.7 ‰). Only the synoptic scale variability is well expressed in
401 the records of $\delta^{18}\text{O}_v$ and d-excess_v with an anticorrelation between both parameters when
402 looking at the 2-year series at hourly resolution ($R^2 = 0.61$ with R^2 being the coefficient of
403 determination for a linear regression). Moreover, $\delta^{18}\text{O}_v$ is most of the time correlated with water
404 vapor mixing ratio ($R^2 = 0.55$ for the 2-year series at hourly resolution).

405 There are a few exceptions to the general correlation between water vapor $\delta^{18}\text{O}$ and water vapor
406 mixing ratio as illustrated in Figure 3. Short periods of a few days are associated with a decrease
407 of the correlation coefficient, R estimated from the correlation between $\delta^{18}\text{O}_v$ and q_v (R is
408 calculated continuously from hourly records on an 8-day moving window). The periods of low
409 R are also often characterized by a negative peak of several ‰ in $\delta^{18}\text{O}_v$, which is not visible in
410 the d-excess_v. During these $\delta^{18}\text{O}_v$ excursions, the general anti-correlation between $\delta^{18}\text{O}_v$ and d-
411 excess_v hence also breaks down. Our study mostly focuses on the 11 most prominent abrupt
412 events highlighted in the $\delta^{18}\text{O}_v$ record (only 10 visible on Figure 3 because of the scale). The
413 11 most abrupt events occurring when correlation coefficient R between $\delta^{18}\text{O}_v$ and d-excess_v is
414 larger than -0.5 are associated with $\delta^{18}\text{O}_v$ negative excursion larger than 3 ‰ (at 6h resolution)
415 over a period of less than 24 h, the length of the event being measured between the mid-slopes
416 of the decrease and subsequent increase of the $\delta^{18}\text{O}_v$. The 11 selected negative excursions occur
417 at a rate larger than -0.5‰ h⁻¹ and the $\delta^{18}\text{O}_v$ increase at the end of each excursion has an
418 amplitude larger than half the amplitude of the corresponding initial decrease.

419

420 **3.2 Model-data comparison**

421



422

423 **Figure 4:** Model-measurement comparison (January – March 2020); a- $\delta^{18}\text{O}_v$ (light blue for
424 data on hourly average, dotted dark blue for data resampled at a 6-hour resolution); b- water
425 vapor mixing ratio from our data set; c- vertical velocity; d- Precipitation amount. The grey
426 shaded areas highlight the negative $\delta^{18}\text{O}_v$ excursions as defined in 3.1.3 (note that in this figure
427 the excursions of the 3rd and 9th of January 2020 are distinct while the distinction could not be
428 done on Figure 3 because of the scale).

429

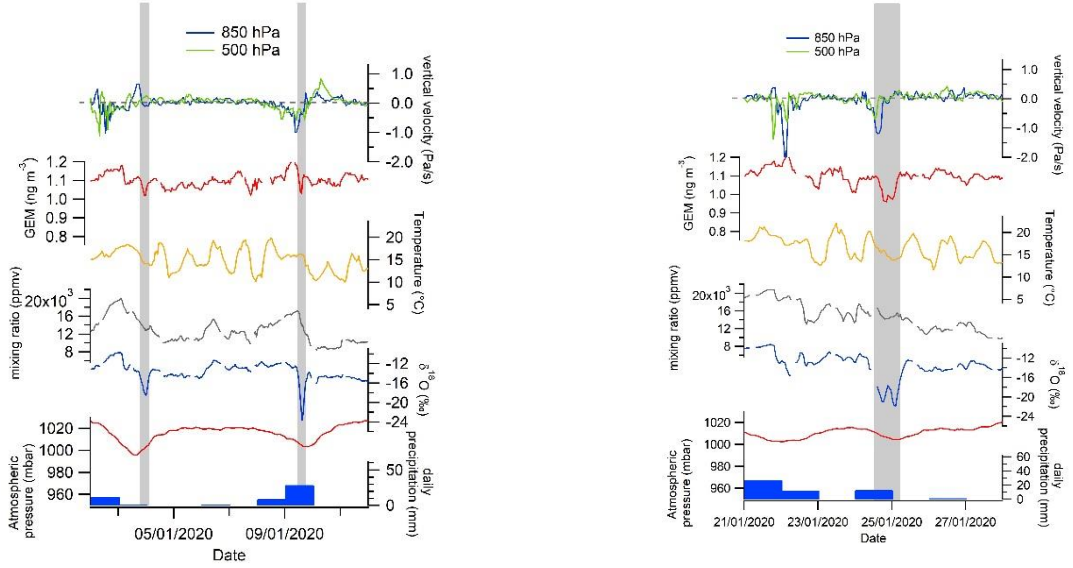
430 We selected a 3-month period (January to March 2020) for the comparison between our dataset
431 and the outputs of the ECHAM6-wiso and LMDZ-iso models. This period has been selected
432 for display because it encompasses 4 out the 11 negative excursions of $\delta^{18}\text{O}_v$, but the extended
433 comparison over the whole 2 years period is displayed in Figure A1. There is an overall
434 agreement between the measured and modelled $\delta^{18}\text{O}_v$ and water vapor mixing ratio (Figure 4).
435 The best agreement over the 3-month series is obtained with the ECHAM6-wiso and LMDZ-
436 iso (LR) models ($R^2 = 0.59 - 0.6$ and $0.87 - 0.90$ respectively for $\delta^{18}\text{O}_v$ and water vapor mixing
437 ratio series) while a slightly less good agreement is observed with the VLR simulation of the
438 LMDZ-iso model ($R^2 = 0.49$ and 0.79 respectively for $\delta^{18}\text{O}_v$ and water vapor mixing ratio
439 series). The same observation can be done on the entire 2-year time series. We also compare
440 the precipitation amount modelled by ECHAM6-wiso and LMDZ-iso to the precipitation
441 amount measured by the MeteoFrance weather station. The correlation between modeled and
442 measured precipitation is close to zero for LMDZ-iso ($R^2 = 0.08 - 0.13$ for VLR - LR) while
443 there is a better agreement when comparing measured precipitation amount to outputs of

444 ECHAM6-wiso ($R^2 = 0.45$). Finally, when focusing on the short term negative $\delta^{18}\text{O}_v$ excursions
445 (Figures 4 and A1), they are in general more strongly expressed in the measurement time series
446 than in the model series. Part of this disagreement can be explained by the fact that the $\delta^{18}\text{O}_v$
447 record has a higher temporal resolution (1h) than the model outputs (3h for LMDZ-iso and 6h
448 for ECHAM6-wiso). However, when interpolating the $\delta^{18}\text{O}_v$ record at a 6h resolution (dotted
449 dark blue), the negative excursions are still clearly visible while not captured by the LMDZ-iso
450 model (Figure 4 and Table 1). When looking at the whole 2-year series, the LMDZ-iso VLR
451 simulation fails to reproduce most of these $\delta^{18}\text{O}_v$ excursions (only the negative excursion of 3rd
452 January, 2020 is reproduced) while the ECHAM6-wiso model is able to capture all the $\delta^{18}\text{O}_v$
453 excursions. The LMDZ-iso LR simulation produces a negative $\delta^{18}\text{O}_v$ excursion over many
454 events with a significantly lesser amplitude than in the data and in the ECHAM6-wiso model
455 (Table 1).

456

457 **4. Discussion**

458 The most remarkable pattern from this 2-year series is the succession of short negative
459 excursions of $\delta^{18}\text{O}_v$ associated with decorrelation between $\delta^{18}\text{O}_v$ and humidity, $\delta^{18}\text{O}_v$ and d-
460 excess_v, and which are highlighted with grey shaded areas in Figure 3, detailed in Figures 5 and
461 A2 and referenced in Table 1. These negative $\delta^{18}\text{O}_v$ excursions always occurred during low
462 pressure periods (atmospheric pressure below 1005 mbar) and we observe the presence of a
463 cold front within a distance of 100 km around Amsterdam Island in a 48h period covering the
464 time of the event (Supplementary Material Figure S1). The focus on the first three months of
465 the series presented in Figure 4 shows that these events are captured by ECHAM6-wiso at 0.9°
466 resolution, but not systematically by LMDZ-iso at 2x1.67° and even less by LMDZ-iso at
467 3.75x1.9° resolution. Such mismatch makes the understanding of the processes at play during
468 these events particularly important to investigate to further improve the performances of
469 atmospheric general circulation models equipped with water isotopes. .



470

471

472 **Figure 5:** Evolution of GEM, $\delta^{18}\text{O}_v$, water vapor mixing ratio, meteorological parameters
473 (surface temperature, surface atmospheric pressure, daily precipitation) measured by the
474 MeteoFrance weather station and vertical velocity from the ERA5 reanalyses at 500 and 850
475 hPa over the three isotopic excursions of January 2020 (a and b) identified on Figure 4. A focus
476 on the other excursions is provided in Figure A2.

477

478 **Table 1:** List of the 11 events associated with both loss of correlation between $\delta^{18}\text{O}_v$ and q_v ,
479 $\delta^{18}\text{O}_v$ and $d\text{-excess}_v$ and negative excursions of $\delta^{18}\text{O}_v$ over 2020-2021. The amplitude of the
480 negative $\delta^{18}\text{O}_v$ anomaly is calculated from the minimum of $\delta^{18}\text{O}_v$ on the record at hourly
481 resolution (at 6h resolution). When the calculated amplitude is smaller than 1 ‰, we indicate
482 only “-”. When the vertical velocity is between -0.25 and 0.25 Pa/s, this is indicated in the table
483 as “~0”.

484

485

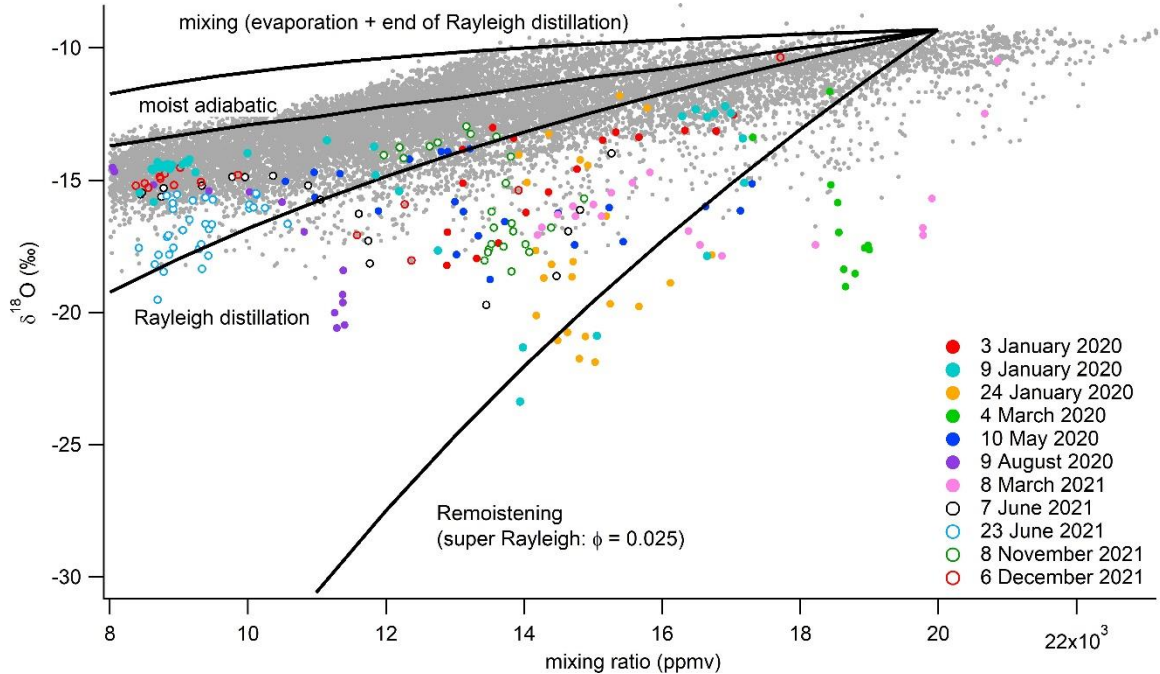
Date of the event	Negative excursion of GEM	Low pressure (< 1005 mbar)	Rain	Relative Humidity at the surface (at minimum $\delta^{18}\text{O}_v$)	vertical velocity from reanalyses (850 hPa)	vertical velocity from reanalyses (500 hPa)	Length of the event (hours)	amplitude of the $\delta^{18}\text{O}_v$ peak in the data (%)	amplitude of the $\delta^{18}\text{O}_v$ peak in ECHAM-wiso (%)	amplitude of the $\delta^{18}\text{O}_v$ peak in LMDZ-iso VLR (%)	amplitude of the $\delta^{18}\text{O}_v$ peak in LMDZ-iso LR (%)
06/12/2021	Yes	Yes	Yes	82%	~0	up	3h	-6 (-5)	-2.3	-	-2
08/11/2021	Yes	Yes	No	85%	~0	~0	17h	-5.5 (-5.5)	-5	-	-4
23/06/2021	No	Yes	Yes	75%	~0	~0	10h	-5.5 (-5.4)	-6	-	-
07/06/2021	No	Yes	Yes	80%	up	~0	9h	-6.5 (-5.8)	-5.8	-	-2
08/03/2021	Yes	Yes	Yes	89%	down	up	20h	-6 (-6)	-4	-	-
09/08/2020	No data	Yes	Yes	87%	down	up	8h	-8 (-6)	-7	-	-2
10/05/2020	Small	Yes	Yes	95%	down	down	14h	-4.9 (-4)	-3	-	-3
04/03/2020	No data	Yes	Yes	98%	up	up	9h	-6.1 (-5.3)	-5	-	-
24/01/2020 (double peak)	Yes	Yes	Yes	93% and 90%	1st peak up and 2nd peak down	1st peak up and 2nd peak down	17h	-7.8 (-7.5)	-4.5	-	-3.5
09/01/2020	Yes	Yes	Yes	94%	up	up	4h	-9 (-4)	-5	-	-
03/01/2020	Yes	Yes	No	90%	down	~0	6h	-2.8 (-2.5)	-2.4	-3	-3.5

486

487 Several hypotheses can be proposed to explain the negative excursions of $\delta^{18}\text{O}_v$. The beginning
 488 of these excursions is associated with a decrease of the water vapor mixing ratio and occurs in
 489 most cases during a precipitation event (Table 1). These events share similarities with negative
 490 $\delta^{18}\text{O}_v$ and $\delta^{18}\text{O}_p$ short events previously observed in temperate regions during a cold front
 491 passage (e.g. Aemisegger et al., 2015). Three possible processes at play to explain such events
 492 have already been listed in previous studies (e.g. Dütsch et al., 2016) (i) local interaction
 493 between the vapor and the rain droplets (rain equilibration and rain evaporation), (ii) vertical
 494 subsidence of water vapor with depleted isotopic composition, or (iii) horizontal advection
 495 through the arrival of a cold front. We explore below how we can gain information on the
 496 different processes using our data set, back trajectories and model-data comparison.

497

4.1 $\delta^{18}\text{O}_v$ vs q_v relationship



499

500 **Figure 6:** Relative evolution of q_v and $\delta^{18}\text{O}_v$ for the different events (colors according to the
501 date as explained in the graph) and for the entire 2 years records (grey). The solid lines are
502 theoretical lines whose equations are detailed in Noone (2012) for different processes
503 (remoistening associated with exchange between rain and water vapor; Rayleigh distillation
504 assuming that all formed condensation is removed from the cloud; moist adiabatic process
505 assuming that liquid condensation stays in the cloud with the water vapor; mixing of water
506 vapor from ocean evaporation around Amsterdam Island and water vapor from the end of the
507 Rayleigh distillation, i.e. high altitude water vapor). The water vapor for the calculation of
508 Rayleigh distillation and for the evaporation above the ocean has a $q_{v,0}$ of 20,000 ppmv and a
509 $\delta^{18}\text{O}_{v,0}$ of -9.3 ‰. The vapor at the end of the distillation line has a water vapor mixing ratio of
510 1,000 ppmv and a $\delta^{18}\text{O}_v$ of -40 ‰.

511

512

513 First, to test the hypothesis of vapor-droplet interactions, we looked at the $\delta^{18}\text{O}_v$ vs q_v
514 distribution following the approach already used by Guilpart et al. (2017) (Figure 6). We
515 acknowledge that our approach is crude and should be taken as a first order approach since we
516 can only look at the water vapor $\delta^{18}\text{O}_v$ vs q_v distribution in the surface layer using adapted
517 boundary conditions while it may be more relevant to look at this relationship in the free
518 troposphere. In general, the $\delta^{18}\text{O}_v$ vs q_v evolution lies on a curve which can be explained by
519 condensation processes (Rayleigh distillation or reversible moist adiabatic process). However,

520 for the 11 events highlighted above, the water vapor $\delta^{18}\text{O}_v$ vs q_v evolution follows an evolution
521 standing below the curve of the $\delta^{18}\text{O}_v$ vs q_v evolution observed for the rest of the series.
522 Although the evolution of the water vapor $\delta^{18}\text{O}_v$ vs q_v is rather abrupt, there is a certain
523 resemblance with the idealized theoretical remoistening curve initially calculated for the free
524 troposphere (Noone, 2012) and adapted here with initial conditions corresponding to the
525 isotopic composition of surface water vapor. Remoistening is described through a modification
526 of the equilibrium fractionation coefficient between water vapor and rain (α_e) so that the
527 effective fractionation factor is $\alpha = (1+\phi) \times \alpha_e$, ϕ being the degree to which α deviates from
528 equilibrium. This effective fractionation coefficient is then introduced in the Rayleigh
529 distillation equation to deduce the link between $\delta^{18}\text{O}_v$ and mixing ratio as:

530
$$\delta^{18}\text{O}_v - \delta^{18}\text{O}_{v,0} = (\alpha - 1) \times \ln(q_v/q_{v,0}) \quad (\text{Eq 8})$$

531 Despite the simplicity of our approach, the fact that the water vapor $\delta^{18}\text{O}_v$ vs q_v evolution lies
532 below the idealized curve for condensation processes supports the depleting effect of vapor-
533 rain interactions for our negative water vapor $\delta^{18}\text{O}_v$ excursions (Noone, 2012; Worden et al.,
534 2007). Surface relative humidity remains relatively high during these events (values given in
535 Table 1 compared to a mean value of 77 %) which favors rain-vapor diffusive exchanges. This
536 interpretation is also supported by the stable d -excess_v during these events.

537

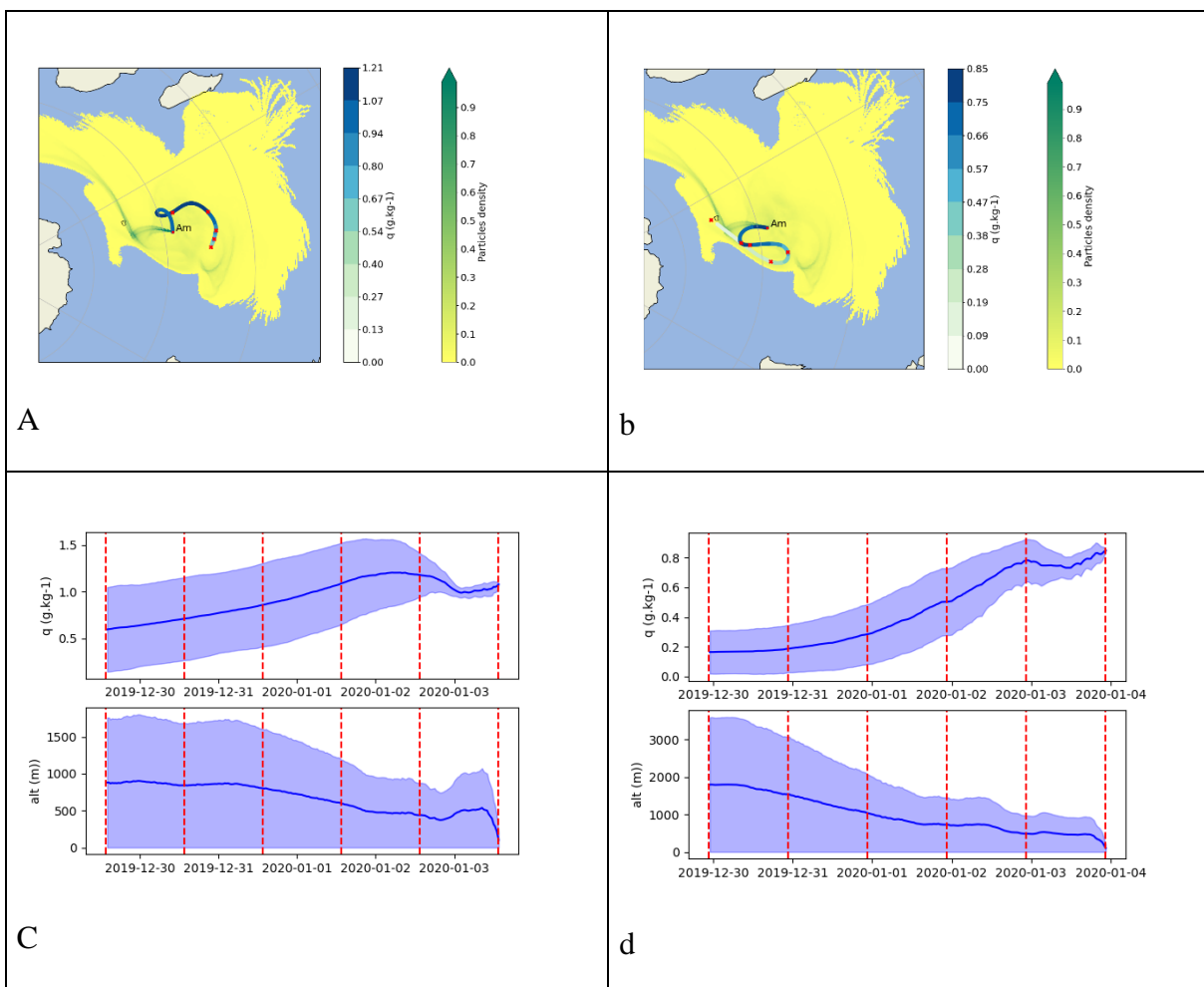
538 **4.2 $\delta^{18}\text{O}_v$ vs GEM relationship**

539 Second, to test the hypothesis of subsidence of air from higher altitude, GEM is used. Indeed,
540 aircraft measurements as well as model simulations demonstrated that the upper
541 troposphere/lower stratosphere is depleted in GEM and enriched in species composed of
542 reactive gaseous mercury and particulate bound mercury (Lyman and Jaffe, 2012; Murphy et
543 al., 2006; Sillman et al., 2007; Swartzendruber et al., 2006, 2008; Talbot et al., 2007, 2008).
544 This leads to lower GEM concentrations than those usually observed when the lowest
545 atmosphere layer is only under marine influence (Angot et al., 2014; Lindberg et al., 2007). The
546 fact that GEM negative excursions are observed in phase with negative $\delta^{18}\text{O}_v$ excursions in
547 most of the events (6 events on a total of 9 events with GEM data, cf Figure 5 and A2, Table 1)
548 suggests that vertical subsidence of water vapor, $\delta^{18}\text{O}$ -depleted by Rayleigh distillation and/or
549 rain-vapor interactions, can have an influence on the observed excursions of $\delta^{18}\text{O}_v$, in
550 agreement with the conclusion of Dütsch et al. (2016).

551

552 **4.3 Back trajectories information**

553 To further explore the processes leading to the decoupling of humidity and $\delta^{18}\text{O}_v$ as well as
 554 sharp negative excursions of $\delta^{18}\text{O}_v$ during the 11 events identified here, we also use information
 555 from the ERA5 reanalyses. In particular, the influence of atmospheric circulation (vertical and
 556 horizontal advection) and moisture origin can be studied through back trajectories. The back
 557 trajectories, presented here for 3 events (Figures 7, A3 and A4), confirm the information from
 558 wind directions that there is no systematic change in the horizontal origin of the trajectories for
 559 the different events. No systematic pattern is identified either in the vertical advection even if
 560 we note that for the event of January 3rd, the average altitude of the envelope of the 5-day back
 561 trajectories increases when comparing the situation before the excursion and the situation when
 562 the most negative $\delta^{18}\text{O}_v$ values are reached. This observation may support the occurrence of
 563 air subsidence as indicated by the GEM record for this particular event (Figure 5).



564

565 **Figure 7** : FLEXPART footprints of 5-day back trajectories for the event of the 3rd-4th of
 566 January. (a) Latitude-longitude projection of the FLEXPART back trajectory footprints for
 567 January 3rd 2020 at 13h30. The yellow to green colors on each grid point of these projections

568 represent the density of particles. The white to blue colors indicate the water vapor mixing
569 ratio along the humidity-weighted average back trajectory. Each red point indicates the
570 location of the average back trajectory for each of the 5 days before the date of the considered
571 event. (b) Same as a for January 3rd 2020 at 22h30. (c) Top shows the evolution of the water
572 vapor mixing ratio of the back trajectories for January 3rd 2020 at 13h30; bottom shows the
573 altitude evolution of the back trajectory for January 3rd 2020 at 13h30. (d) same as (c) for
574 January 3rd 2020 at 22h30.

575

576 The subsidence over the different events can better be studied from the vertical velocity from
577 the ERA5 reanalyses (Figure 4 and A1). Subsidence (positive vertical velocity) is not
578 systematically associated with negative $\delta^{18}\text{O}_v$ excursions: subsidence at either 850 hPa or 500
579 hPa is observed only for 5 events over 11 (Table 1). In 4 cases, there is rather an ascending
580 movement of the atmospheric air associated with the rain event. In the other cases, there is no
581 clear vertical movement. However, we note that when negative $\delta^{18}\text{O}_v$ excursions are not
582 concomitant with subsidence, they occur at the end of an ascending movement which is
583 generally followed by subsidence (Figures A1 and A2).

584

585 **4.4 Model – data comparison and atmospheric dynamic**

586 With the information gathered above, both subsidence and isotopic depletion associated with
587 rain occurrence and further interaction between droplets and water vapor can explain the
588 negative excursions of $\delta^{18}\text{O}_v$. We note however that the data gathered so far do not permit to
589 provide a simple and unique explanation. Neither subsidence nor rain systematically occurred
590 for each of the $\delta^{18}\text{O}_v$ excursion. Still, the fact that at least ECHAM6-wiso is able to reproduce
591 every negative $\delta^{18}\text{O}_v$ excursion (whether they are associated or not with subsidence or rain-
592 water vapor reequilibration) shows that (1) the patterns of atmospheric water cycle are correctly
593 reproduced, a validation which can be performed using humidity and precipitation data for
594 some aspects but benefits from water isotopes implementation for the residence time of water
595 and (2) the isotopic processes are correctly implemented in this model. Such abrupt $\delta^{18}\text{O}_v$ events
596 can hence be used as a test bed of the performances of water isotopes enabled general circulation
597 models.

598 To further explore the $\delta^{18}\text{O}_v$ data-model comparison and associated processes, we compare the
599 performances of the ECHAM6-wiso and the LMDZ-iso models over the first months of 2020
600 in terms of atmospheric dynamics (Figures 4 and A1). First and as expected because of the

601 nudging, the two models reproduce rather well the evolution of the vertical velocity of the
602 ERA5 reanalyses with a stronger ascent for the model predicting the strongest precipitation
603 amount (e.g. LMDZ-iso for January 24th 2020). The event of January 3rd is the only one
604 reproduced by both ECHAM6-wiso and the two versions of the LMDZ-iso model: the three
605 simulations show a clear subsidence over the isotopic event and a clear negative $\delta^{18}\text{O}_v$
606 excursion. For the other events, neither LMDZ-iso nor ECHAM6-wiso show a clear signal of
607 subsidence neither at 500 nor at 850 hPa (not shown). However, the horizontal distribution of
608 vertical velocity obtained with ECHAM6-wiso and LMDZ-iso are significantly different
609 (Figure 8 for the event of the 9th of January, Supplementary Material Figures S2 and S3 for the
610 other events). While the LMDZ-iso modelled vertical velocity displays a rather strong
611 homogeneity on the vertical axis, ECHAM6-wiso modelled vertical velocity highlights
612 subsidence of air below the ascending column, with the maximum of negative $\delta^{18}\text{O}_v$ anomaly
613 at the surface located just at the limit between ascendance and subsidence (between 75°E and
614 77°E in Figure 8c). This subsidence of depleted $\delta^{18}\text{O}_v$ below the ascending column is
615 responsible for the sharp negative $\delta^{18}\text{O}_v$ excursion in the ECHAM6-wiso model. The fact that
616 subsidence of air occurs just below uplifted air, at the limit between ascendance and subsidence
617 (Figure 8k and Supplementary Material Figure S2), permits to reconcile the GEM data
618 suggesting subsidence and the sign of the vertical velocity of the ERA5 reanalyses at
619 Amsterdam Island suggesting that many excursions start with ascendance. Since the isotope
620 implementation was done similarly in the two models, the reason why the LMDZ-iso model
621 does not reproduce the water isotopic anomaly is its too coarse resolution as also supported by
622 the comparison between performances of the LMDZ-iso model at low resolution and very low
623 resolution for the event of the 24th of January (Table 1 and Figure 4). As already pointed by
624 Ryan et al. (2000), a fine resolution is necessary to correctly simulate front dynamics and we
625 extend this result here to the high resolution temporal patterns of surface $\delta^{18}\text{O}_v$.

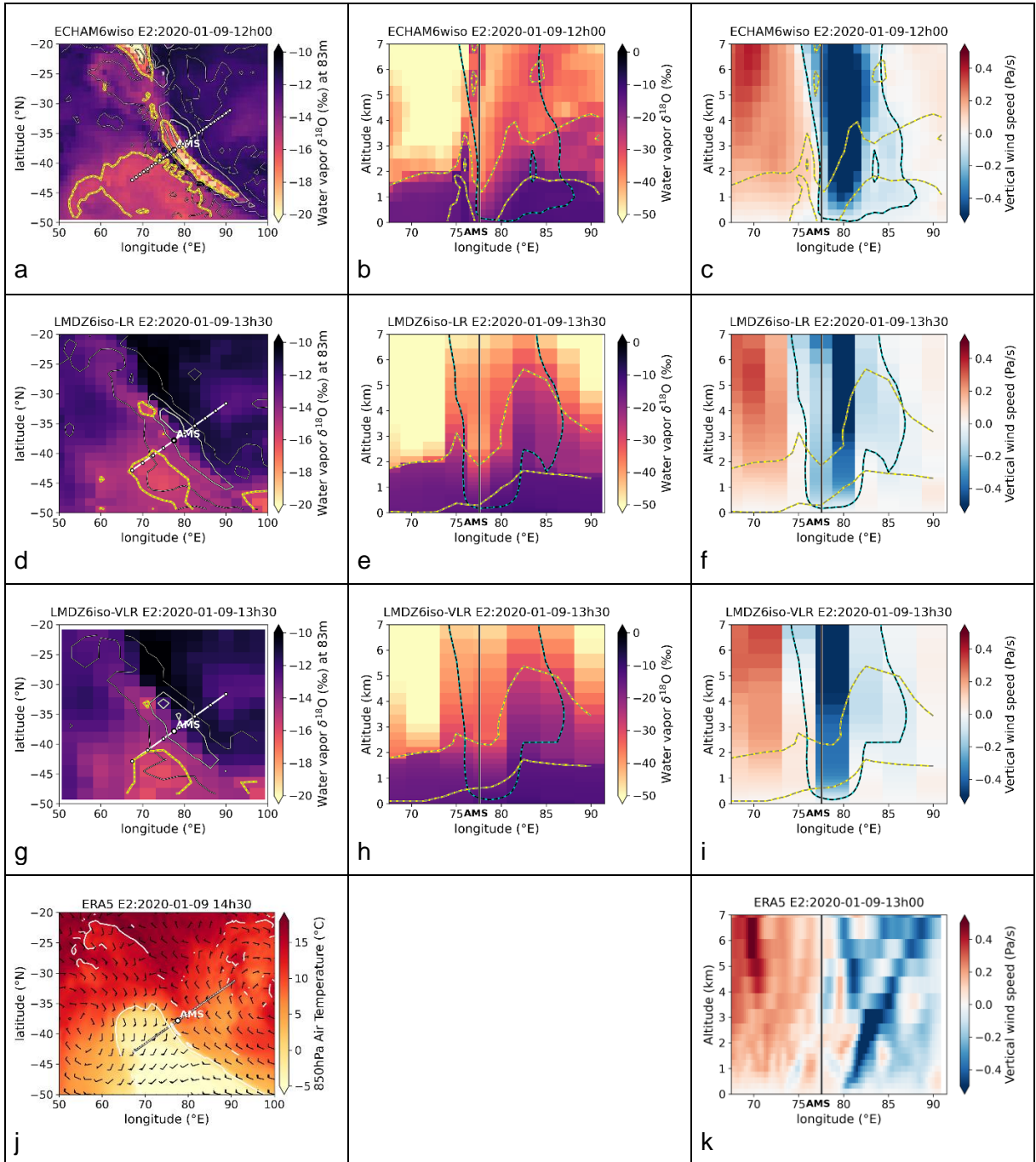
626

627 **4.5 Synthesis**

628 Figure 9 summarizes the proposed mechanism for negative $\delta^{18}\text{O}_v$ excursions as inferred from
629 our data – model comparison when there is a clear rain event. A rain event is associated with a
630 strong ascending column in which $\delta^{18}\text{O}_v$ is depleted by progressive precipitation during the
631 ascent and by interaction between rain and water vapor. This ascending column is generally
632 associated with a cold front moving from South-West to North-Est (Fig. 8j and Supplementary

633 Material S1), with subsidence and $\delta^{18}\text{O}_v$ depleted air at the rear of the front (Fig. 8 and
634 Supplementary Material S2 and S3).

635

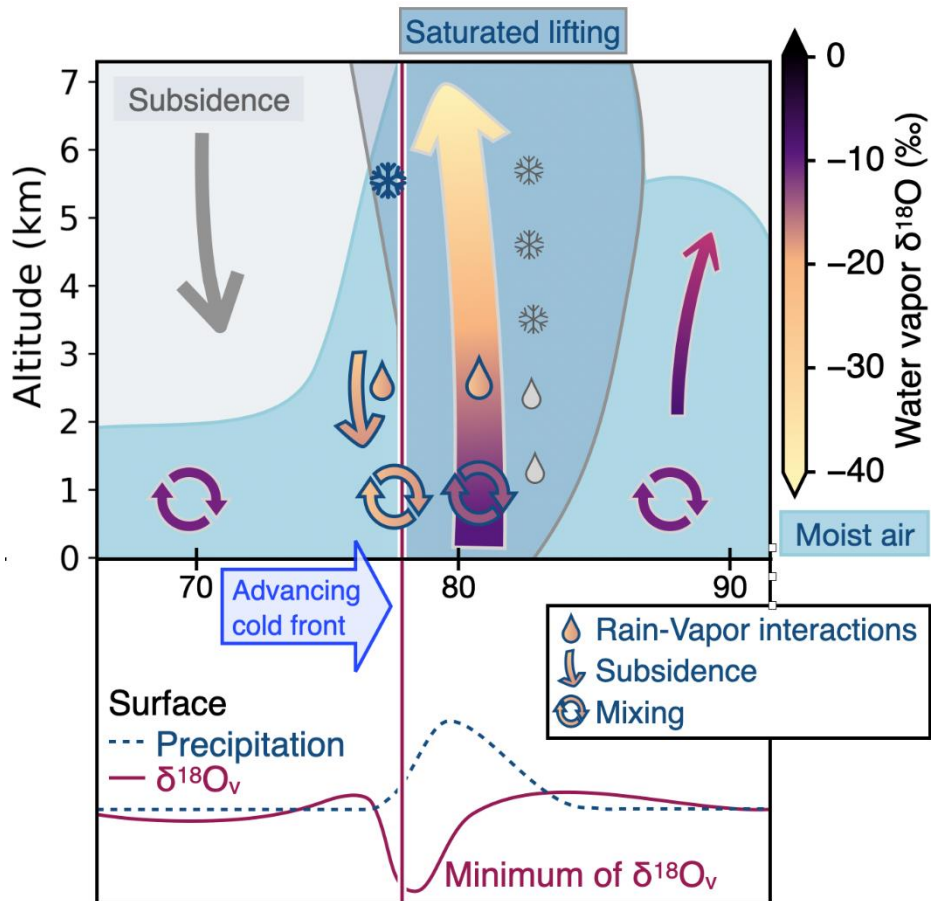


636

637

Figure 8: Modelled $\delta^{18}\text{O}_v$ and vertical velocity for the event of January 9th 2020. (a) Surface air $\delta^{18}\text{O}_v$ (~ 83 m, latitude vs longitude), with yellow line indicating -15 ‰ contour level and grey lines indicating precipitation contours at $0.5, 10$, and 50 mm day^{-1} (thin, medium and thick lines respectively); (b) $\delta^{18}\text{O}_v$ plotted on a vertical cross-section (altitude vs longitude) along the transect indicated by the white line on panel (a), with yellow lines indicating $\delta^{18}\text{O}_v$ contours at -30 ‰ and -15 ‰ , blue lines indicating the contour of -0.05 Pa s^{-1} vertical velocity (ascendance), and the vertical black line denoting the longitude of Amsterdam Island; (c) Vertical velocity plotted on a vertical cross-section as for (b), with same contour lines. (a), (b)

645 and (c) are drawn using outputs of the ECHAM6-wiso model ; (d), (e) and (f) are the same as
 646 (a), (b) and (c) but obtained from the LMDZ-iso model at low resolution (LR) ; (g), (h) and (i)
 647 are the same as (a), (b) and (c) but obtained from the LMDZ-iso model at very low resolution
 648 (VLR). (j) ERA5 air temperature at 850 hPa, with white lines marking front locations (see
 649 Supplementary Material S1); (k) ERA5 vertical velocity plotted on a vertical cross-section
 650 (altitude vs longitude) along the transect indicated by the black dotted line on panel (j).
 651



652
 653 **Figure 9:** Scheme of the mechanism explaining the sharp negative excursion of $\delta^{18}\text{O}_v$ recorded
 654 at the surface for cold front events associated with precipitation. The scheme is based on the
 655 profile modelled by ECHAM6-wiso for event of January 9th 2020 (see Supplementary Material
 656 Figure S5 for other events). The top panel show the altitude vs longitude dynamics of air masses
 657 with vertical saturated lifting in the center and subsidence at the rear of the lifting. The bottom
 658 panel shows the associated evolution of $\delta^{18}\text{O}_v$ and precipitations on the same longitude scale
 659 than on the upper panel.
 660

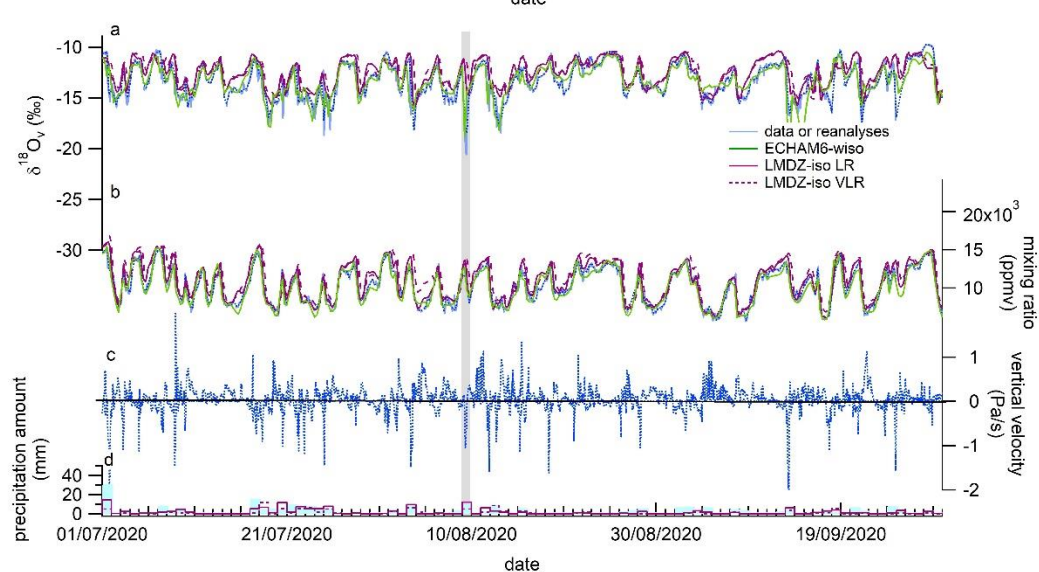
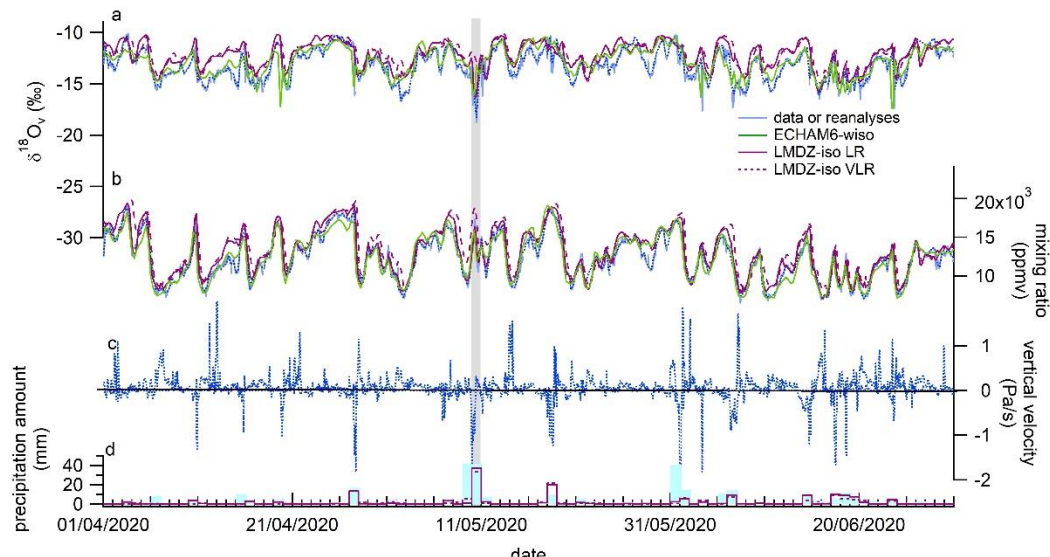
661 **5. Conclusion**

662 We presented here the first water vapor isotopic record over 2 years on Amsterdam Island. The
663 water vapor isotopic variations follow at first order the variations of water vapor mixing ratio
664 as expected for such a marine site. Superimposed to this variability, we have evidenced 11
665 periods of a few hours characterized by the occurrence of one or two abrupt negative excursions
666 of $\delta^{18}\text{O}_v$ while the correlation between $\delta^{18}\text{O}_v$ and water vapor mixing ratio does not hold. These
667 negative excursions are often occurring toward the end of precipitation events. They are most
668 of the time occurring during a decrease in water vapor mixing ratio. Representation of these
669 short events is a challenge for the atmospheric components of Earth System Models equipped
670 with water isotopes and we found that the ECHAM6-wiso model was able to reproduce most
671 of the sharp negative $\delta^{18}\text{O}_v$ excursions while the LMDZ-iso model at low (very low) resolution
672 was only able to reproduce 7 (1) of the negative excursions. The good agreement between
673 modeled and measured $\delta^{18}\text{O}_v$ when using ECHAM6-wiso validates the physics processes
674 within the ECHAM6-wiso model as well as the implemented physics of water isotopes.
675 Using previous modeling studies as well as information provided by (1) the confrontation with
676 other data sources (GEM, meteorology) obtained in parallel on this site, (2) back trajectory
677 analyses and (3) the outputs of the two models ECHAM6-wiso and LMDZ-iso, we conclude
678 that the most plausible explanations for such events are rain-vapor interactions and subsidence
679 at the rear of a precipitation event. Both can be combined, since rain vapor interactions can help
680 maintaining moist conditions in subsidence regions.
681 This study highlights the added value of combining different data from a surface atmospheric
682 observatory to understand the dynamics of the atmospheric circulation, e.g. subsidence in the
683 higher atmosphere. These 2-year records are also a good benchmark for model evaluation. We
684 have especially shown that the isotopic composition of water vapor measured at the surface is
685 a powerful tool to test the vertical dynamic of atmospheric models and the implementation of
686 water isotopes for those that are equipped with them. In our case, we used it to test different
687 horizontal resolutions which influence the representativity of the vertical dynamics and have
688 important implication in the simulation of surface variations of water vapor $\delta^{18}\text{O}_v$. Our study
689 highlights the importance to have high-resolution models (e.g. mesoscale models) equipped
690 with isotopes to further study such abrupt isotopic events.

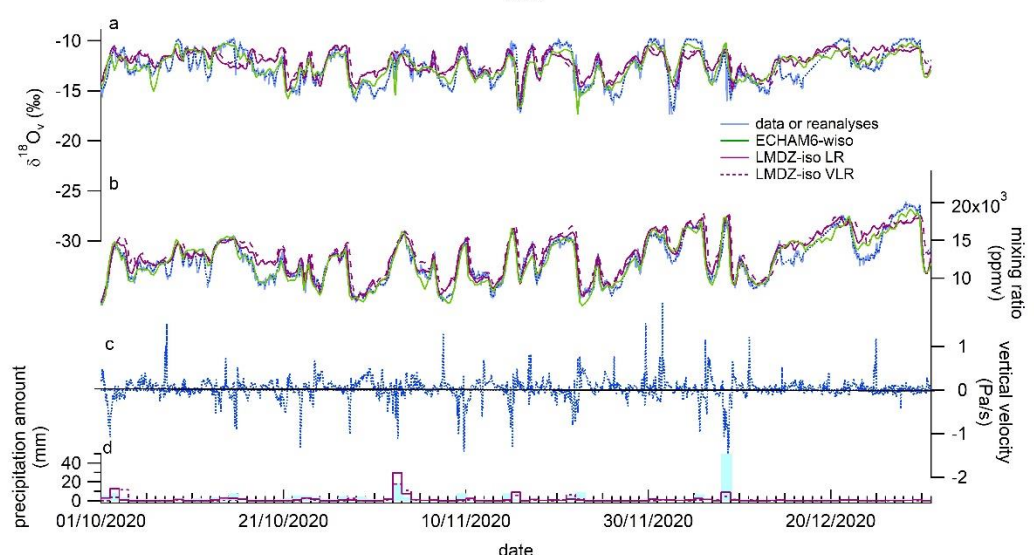
691
692

693 Appendices:

694

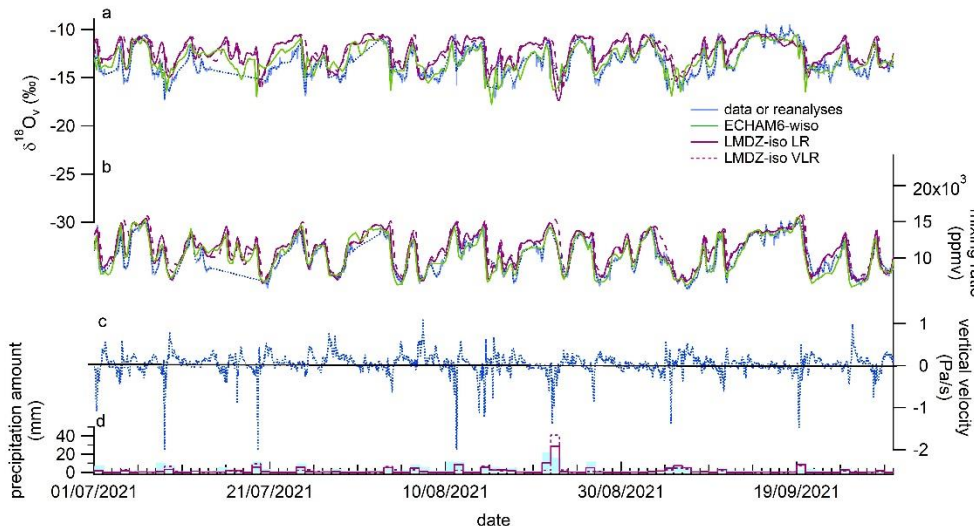
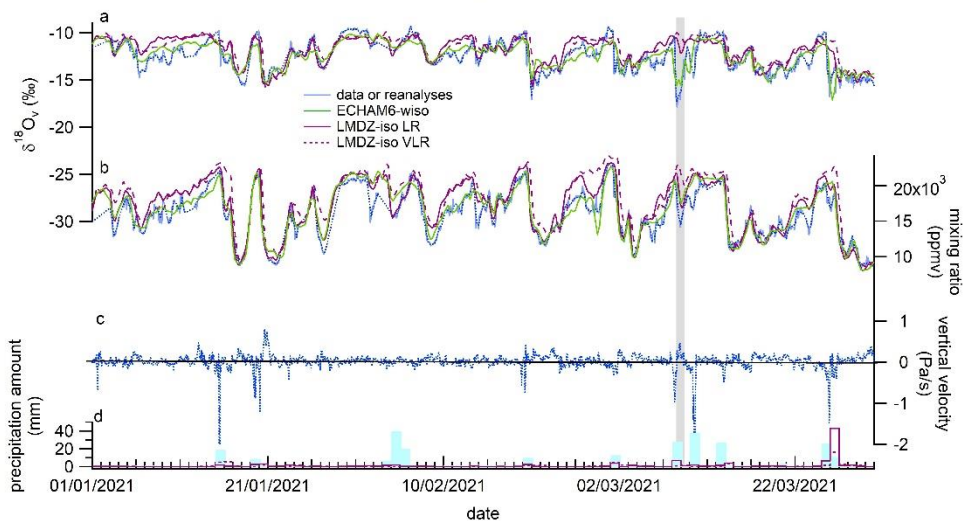
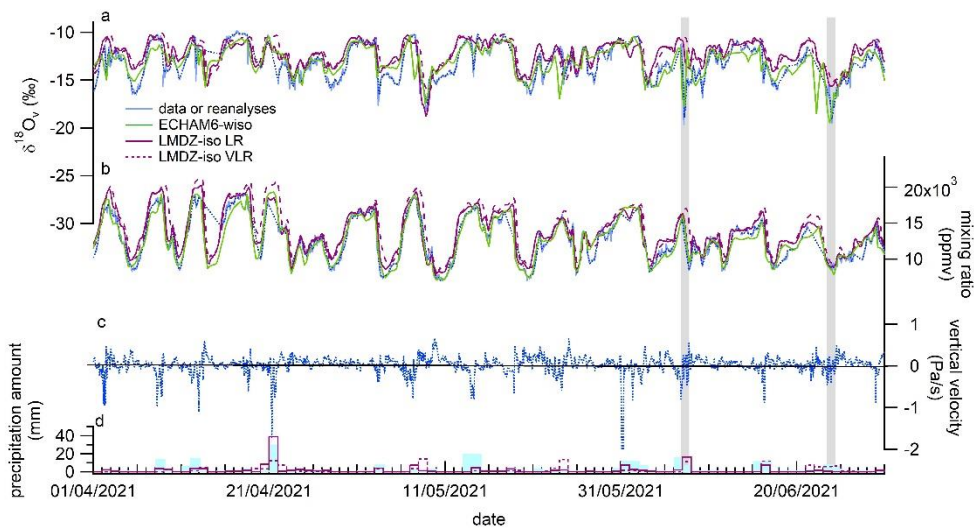


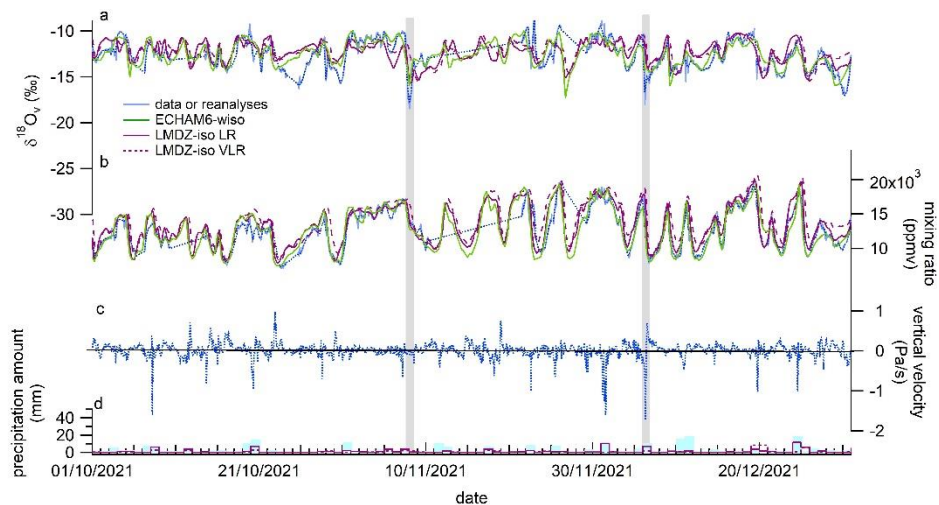
696



697

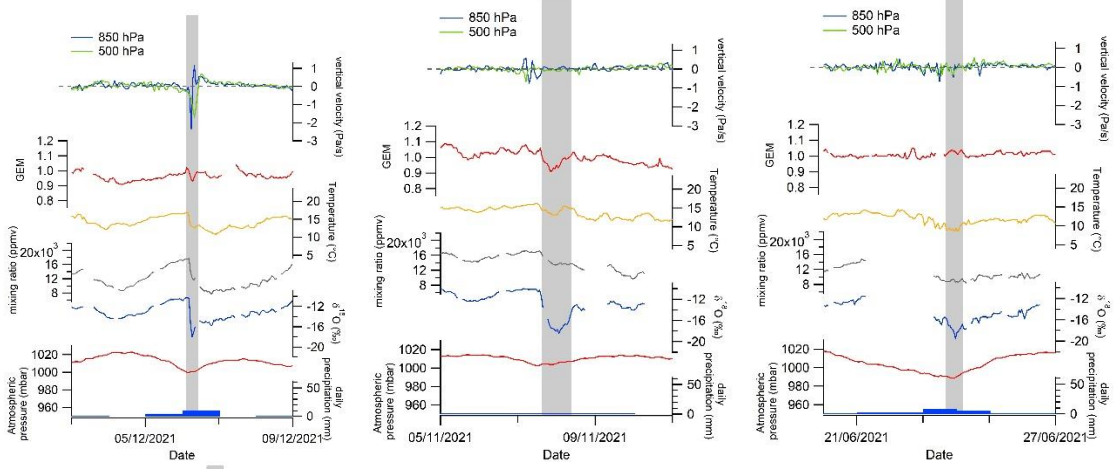
698



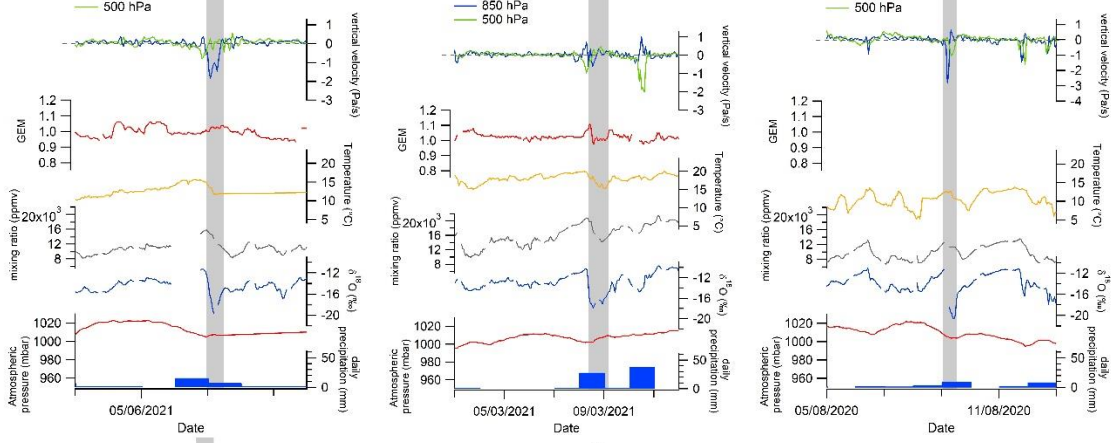


702
 703
 704
 705 **Figure A1:** Model-measurement comparison (April 2020 – December 2021); a- $\delta^{18}\text{O}_v$ (light blue for
 706 data on hourly average, dark blue for data resampled at a 6-hour resolution); b- water vapor mixing ratio
 707 from our data set; c- vertical velocity; d- Precipitation amount. The grey shadings highlight the negative
 708 $\delta^{18}\text{O}_v$ excursions.
 709

710



711



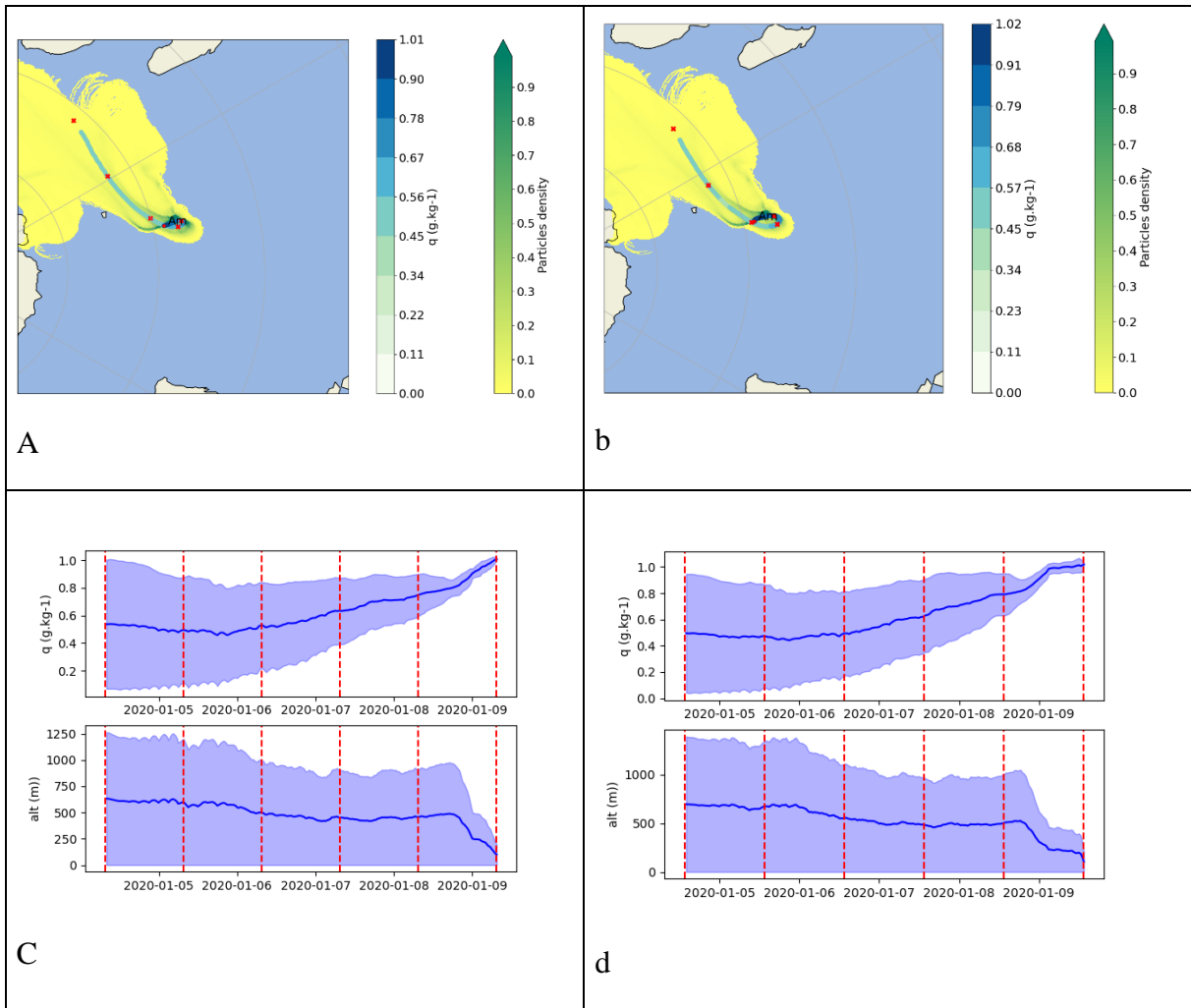
712

713

714 **Figure A2 :** Evolution of GEM, $\delta^{18}\text{O}_v$, water vapor mixing ratio, meteorological parameters
 715 (surface temperature, surface atmospheric pressure, daily precipitation) measured by the
 716 MeteoFrance weather station and vertical velocity from the ERA5 reanalyses at 500 and 850
 717 hPa over the isotopic excursions between March 2020 and December 2021 (a to i).

718

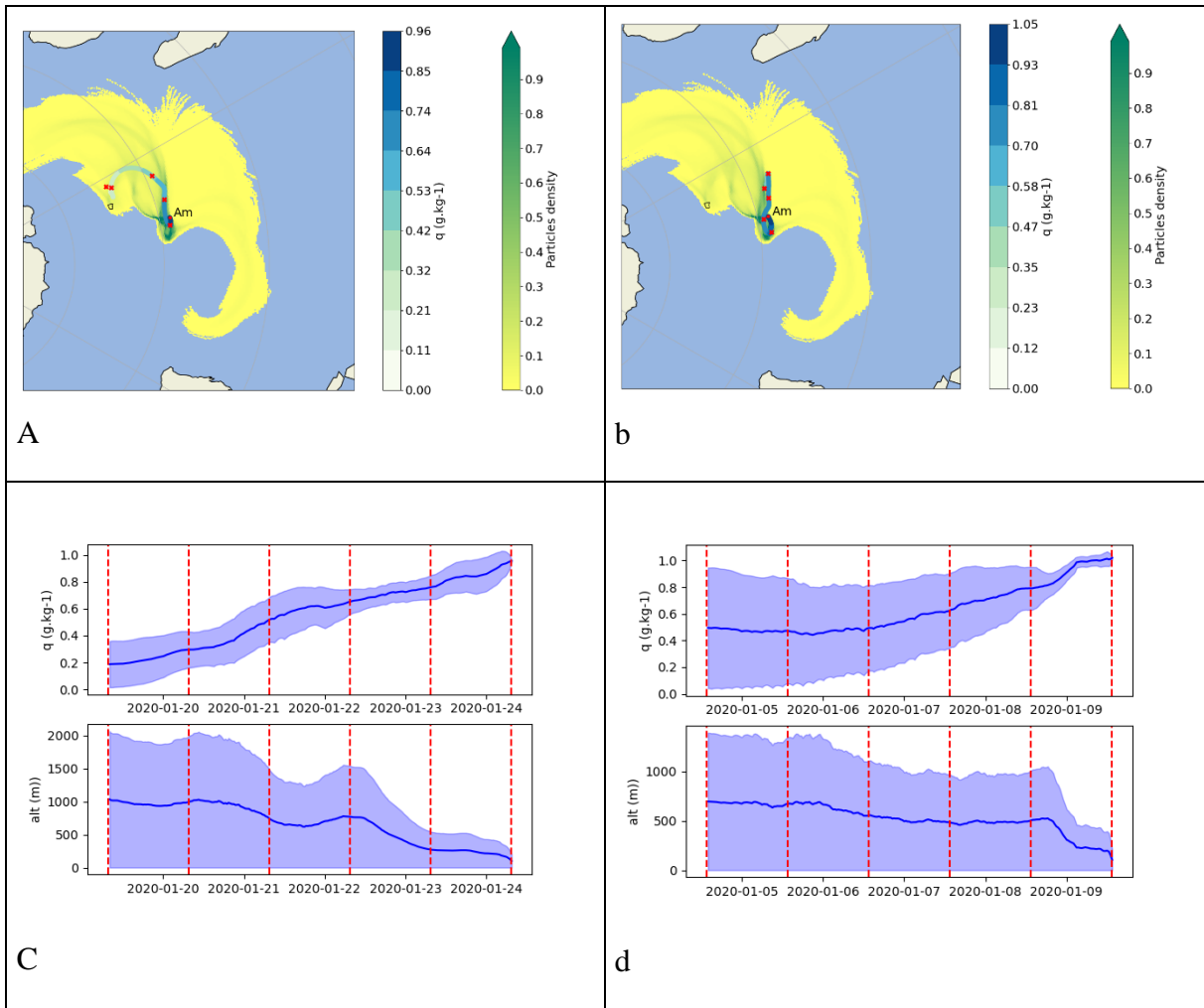
719



720
721

722 **Figure A3:** FLEXPART footprints of 5-day back trajectories for the event of January 9th 2020.
 723 Panel (a) Latitude-longitude projection of the FLEXPART back trajectory footprint for January
 724 9th 2020 at 7h30. The yellow to green colors on each grid point of these projections represent
 725 the density of particles. The white to blue colors indicate the water vapor mixing ratio on the
 726 humidity weighted average back-trajectory. Each red point indicates the location of the average
 727 back-trajectory for each of the 5 days before the date of the considered event. Panel (b) Same
 728 as a for January 9th 2020 at 13h30. Panel (c) Top shows the evolution of the water vapor mixing
 729 ratio of the back trajectories for January 9th 2020 at 7h30; bottom shows the altitude evolution
 730 of the back trajectory for January 9th 2020 at 7h30. Panel (d) same as panel (c) for January 9th
 731 2020 at 13h30.

732



733
734

735 **Figure A4:** FLEXPART footprints of 5-day back trajectories for the event of January 21st 2020.
 736 (a) Latitude-longitude projection of the FLEXPART back trajectory footprint for January 21st
 737 2020 at 7h30. The yellow to green colors on each grid point of these projections represent the
 738 density of particles. The white to blue colors indicate the water vapor mixing ratio on the
 739 humidity weighted average back-trajectory. Each red point indicates the location of the average
 740 back-trajectory for each of the 5 days before the date of the considered event. (b) Same as a for
 741 January 21st 2020 at 13h00. (c) Top shows the evolution of the water vapor mixing ratio of the
 742 back trajectories for January 21st 2020 at 7h30; bottom shows the altitude evolution of the back
 743 trajectory for January 21st 2020 at 7h30. (d) same as (c) for January 21st 2020 at 13h00.

744
745
746
747

748 **Data availability:** AMS L2 GEM data (<https://doi.org/10.25326/168>) are freely available
749 (Magand and Dommergue, 2022) at <https://gmos.aeris-data.fr/> from national GMOS-FR
750 website data portal coordinated by IGE (Institut des Géosciences de l'Environnement,
751 Grenoble, France; technical PI: Olivier Magand) with the support of the French national
752 AERIS-SEDOO partners, data and services center for the atmosphere (last access: 08 December
753 2022). Hg species measurements belong to international monitoring networks
754 (<http://www.gos4m.org/>). Water isotopic data and modeling outputs are available on the
755 Zenodo platform (<https://zenodo.org/record/8164392>; <https://zenodo.org/record/8160871>).

756

757 **Acknowledgements:** We deeply thank all overwintering staff at AMS and the French Polar
758 Institute Paul-Emile Victor (IPEV) staff and scientists who helped with the setup and
759 maintenance of the experiment at AMS in the framework of the GMOStral-1028 IPEV
760 program, the ICOS-416 program and the ADELISE-1205 IPEV program. Amsterdam Island
761 Hg₀ data, accessible in national GMOS-FR website data portal were collected via instruments
762 coordinated by the IGE-PTICHA technical platform dedicated to atmospheric chemistry field
763 instrumentation. GMOS-FR data portal is maintained by the French national center for
764 Atmospheric data and services AERIS, which is acknowledged by the authors. The LMDZ-iso
765 simulation were performed thanks to granted access to the HPC resources of IDRIS under the
766 allocations 2022-AD010114000 and 2022-AD010107632R1 and made by GENCI. We deeply
767 thank Sébastien Nguyen (CEA, LSCE) for his help and support in running LMDZiso
768 simulation.

769

770 **Funding:** This work benefited from the IPSL-CGS EUR and was supported by a grant from
771 the French government under the Programme d'Investissements d'avenir, reference ANR-11-
772 IDEX-0004-17-EURE-0006, managed by the Agence Nationale de la Recherche. This project
773 has also been supported by the LEFE IMAGO project ADELISE. Amsterdam Island GEM data,
774 accessible in national GMOS-FR website data portal have been collected with funding from
775 European Union 7th Framework Programme project Global Mercury Observation System
776 (GMOS 2010-2015 Nr. 26511), the French Polar Institute IPEV via GMOStral-1028 IPEV
777 program since 2012, the LEFE CHAT CNRS/INSU (TOPMMODEL project, Nr. AO2017-
778 984931) and the H2020 ERA-PLANET (Nr. 689443) iGOSP program. This work is part of the
779 AWACA project that has received funding from the European Research Council (ERC) under
780 the European Union's Horizon 2020 research and innovation programme (Grant agreement No.
781 951596). The ERA5 reanalyses files for the ECHAM6-wiso nudging have been provided by

782 the German Climate Computing Center (DKRZ). The ECHAM6-wiso simulations have been
783 performed with support of the Alfred Wegener Institute (AWI) supercomputing centre.

784

785 **Author contributions:** AL designed the study and analyzed the data together with FV, CS, EF,
786 OM. OC installed the water vapor isotopic analyzer in Amsterdam Island and OJ was in charge
787 of the data calibration. BM and FP performed the measurements of the isotopic composition of
788 the precipitation samples. CA analyzed the modeling outputs, realized most of the simulations
789 and performed model-data analyses. CLDS performed the back trajectory analyses with help
790 from MC. OM, AD and YB provided expertise on GEM analyses and interpretation. AC, CR,
791 ND and MW provided model simulations. AL wrote the paper with contribution of all
792 coauthors.

793

794 **Competing interests:** One of the coauthors (AD) is a member of the editorial board of
795 Atmospheric Chemistry and Physics.

796

797

798 **References**

799 Aemisegger, F., Sturm, P., Graf, P., Sodemann, H., Pfahl, S., Knohl, A., and Wernli, H.: Measuring
800 variations of d18O and d2H in atmospheric water vapour using two commercial laser-based
801 spectrometers: an instrument characterisation study, *Atmospheric Measurement Techniques*, 5, 1491–
802 1511, <https://doi.org/10.5194/amt-5-1491-2012>, 2012.

803 Aemisegger, F., Spiegel, J., Pfahl, S., Sodemann, H., Eugster, W., and Wernli, H.: Isotope
804 meteorology of cold front passages: A case study combining observations and modeling, *Geophysical*
805 *Research Letters*, 42, 5652–5660, 2015.

806 Angot, H., Barret, M., Magand, O., Ramonet, M., and Dommergue, A.: A 2-year record of
807 atmospheric mercury species at a background Southern Hemisphere station on Amsterdam Island,
808 *Atmospheric Chemistry and Physics*, 14, 11461–11473, 2014.

809 Angot, H., Dion, I., Vogel, N., Legrand, M., Magand, O., and Dommergue, A.: Multi-year record of
810 atmospheric mercury at Dumont d'Urville, East Antarctic coast: continental outflow and oceanic
811 influences, *Atmospheric Chemistry and Physics*, 16, 8265–8279, 2016.

812 Ansari, M. A., Noble, J., Deodhar, A., and Kumar, U. S.: Atmospheric factors controlling the stable
813 isotopes ($\delta^{18}\text{O}$ and $\delta^2\text{H}$) of the Indian summer monsoon precipitation in a drying region of Eastern
814 India, *Journal of Hydrology*, 584, 124636, 2020.

815 Arias, P., Bellouin, N., Coppola, E., Jones, R., Krinner, G., Marotzke, J., Naik, V., Palmer, M.,
816 Plattner, G.-K., Rogelj, J., and others: Climate Change 2021: the physical science basis. Contribution
817 of Working Group I to the Sixth Assessment Report of the Intergovernmental Panel on Climate
818 Change; technical summary, 2021.

819 Bailey, A., Aemisegger, F., Villiger, L., Los, S. A., Reverdin, G., Quiñones Meléndez, E.,
820 Acquistapace, C., Baranowski, D. B., Böck, T., Bony, S., Bordsdorff, T., Coffman, D., de Szoëke, S.
821 P., Diekmann, C. J., Dütsch, M., Ertl, B., Galewsky, J., Henze, D., Makuch, P., Noone, D., Quinn, P.
822 K., Rösch, M., Schneider, A., Schneider, M., Speich, S., Stevens, B., and Thompson, E. J.: Isotopic
823 measurements in water vapor, precipitation, and seawater during EUREC⁴A, *Earth System Science*
824 *Data*, 15, 465–495, <https://doi.org/10.5194/essd-15-465-2023>, 2023.

825 Benetti, M., Reverdin, G., Pierre, C., Merlivat, L., Risi, C., Steen-larsen, H. C., and Vimeux, F.:
826 *Journal of Geophysical Research: Atmospheres* during evaporation, 584–593,
827 <https://doi.org/10.1002/2013JD020535>. Received, 2014.

828 Benetti, M., Aloisi, G., Reverdin, G., Risi, C., and Sèze, G.: Importance of boundary layer mixing for
829 the isotopic composition of surface vapor over the subtropical North Atlantic Ocean, *Journal of*
830 *Geophysical Research: Atmospheres*, 120, 2190–2209, 2015.

831 Bhattacharya, S. K., Sarkar, A., and Liang, M.-C.: Vapor isotope probing of typhoons invading the
832 Taiwan region in 2016, *Journal of Geophysical Research: Atmospheres*, 127, e2022JD036578, 2022.

833 Bloom, N. and Fitzgerald, W. F.: Determination of volatile mercury species at the picogram level by
834 low-temperature gas chromatography with cold-vapour atomic fluorescence detection, *Analytica*
835 *Chimica Acta*, 208, 151–161, 1988.

836 Bonne, J. L., Behrens, M., Meyer, H., Kipfstuhl, S., Rabe, B., Schönicke, L., Steen-Larsen, H. C., and
837 Werner, M.: Resolving the controls of water vapour isotopes in the Atlantic sector, *Nature*
838 *Communications*, 10, 1–10, <https://doi.org/10.1038/s41467-019-09242-6>, 2019.

839 Boucher, O., Servonnat, J., Albright, A. L., Aumont, O., Balkanski, Y., Bastrikov, V., Bekki, S.,
840 Bonnet, R., Bony, S., Bopp, L., Braconnot, P., Brockmann, P., Cadule, P., Caubel, A., Cheruy, F.,

841 Codron, F., Cozic, A., Cugnet, D., D'Andrea, F., Davini, P., de Lavergne, C., Denvil, S., Deshayes, J.,
842 Devilliers, M., Ducharme, A., Dufresne, J.-L., Dupont, E., Éthé, C., Fairhead, L., Falletti, L., Flavoni,
843 S., Foujols, M.-A., Gardoll, S., Gastineau, G., Ghattas, J., Grandpeix, J.-Y., Guenet, B., Guez, E.,
844 Lionel, Guilyardi, E., Guimberteau, M., Hauglustaine, D., Hourdin, F., Idelkadi, A., Joussaume, S.,
845 Kageyama, M., Khodri, M., Krinner, G., Lebas, N., Levavasseur, G., Lévy, C., Li, L., Lott, F., Lurton,
846 T., Luyssaert, S., Madec, G., Madeleine, J.-B., Maignan, F., Marchand, M., Marti, O., Mellul, L.,
847 Meurdesoif, Y., Mignot, J., Musat, I., Ottlé, C., Peylin, P., Planton, Y., Polcher, J., Rio, C., Rochetin,
848 N., Rousset, C., Sepulchre, P., Sima, A., Swingedouw, D., Thiéblemont, R., Traore, A. K.,
849 Vancoppenolle, M., Vial, J., Vialard, J., Viovy, N., and Vuichard, N.: Presentation and Evaluation of
850 the IPSL-CM6A-LR Climate Model, *Journal of Advances in Modeling Earth Systems*, 12,
851 e2019MS002010, <https://doi.org/10.1029/2019MS002010>, 2020.

852 Bréant, C., Leroy Dos Santos, C., Agosta, C., Casado, M., Fourré, E., Goursaud, S., Masson-Delmotte, V., Favier, V., Cattani, O., Prié, F., Golly, B., Orsi, A., Martinerie, P., and Landais, A.: Coastal water vapor isotopic composition driven by katabatic wind variability in summer at Dumont d'Urville, coastal East Antarctica, *Earth and Planetary Science Letters*, 514, 37–47, <https://doi.org/10.1016/j.epsl.2019.03.004>, 2019.

853 Brooks, S.; Ren, X. R.; Cohen, M.; Luke, W. T.; Kelley, P.; Artz, R.; Hynes, A.; Landing, W.; Martos, B. Airborne vertical profiling of mercury speciation near Tullahoma, TN, USA *Atmosphere* 2014, 5 (3) 557– 574 DOI: 10.3390/atmos5030557.

854 855 856

857 Casado, M., Landais, A., Masson-Delmotte, V., Gentron, C., Kerstel, E., Kassi, S., Arnaud, L., Picard, G., Prie, F., Cattani, O., Steen-Larsen, H.-C., Vignon, E., and Cermak, P.: Continuous measurements of isotopic composition of water vapour on the East Antarctic Plateau, *Atmospheric Chemistry and Physics*, 16, <https://doi.org/10.5194/acp-16-8521-2016>, 2016.

858 859 860

861 Cauquoin, A. and Werner, M.: High-Resolution Nudged Isotope Modeling With ECHAM6-Wiso: Impacts of Updated Model Physics and ERA5 Reanalysis Data, *Journal of Advances in Modeling Earth Systems*, 13, e2021MS002532, <https://doi.org/10.1029/2021MS002532>, 2021.

862 863 864

865 Cauquoin, A., Werner, M., and Lohmann, G.: Water isotopes -- climate relationships for the mid-Holocene and preindustrial period simulated with an isotope-enabled version of MPI-ESM, *Climate of the Past*, 15, 1913–1937, <https://doi.org/10.5194/cp-15-1913-2019>, 2019.

866 867

868 Cauquoin, A., Werner, M., and Lohmann, G.: Isotopic Variations in Meteoric Waters, *Science*, 133, 1702–1703, <https://doi.org/10.1126/science.133.3465.1702>, 1961.

869 870 871

872 Dahinden, F., Aemisegger, F., Wernli, H., Schneider, M., Diekmann, C. J., Ertl, B., Knippertz, P., Werner, M., and Pfahl, S.: Disentangling different moisture transport pathways over the eastern subtropical North Atlantic using multi-platform isotope observations and high-resolution numerical modelling, *Atmospheric Chemistry and Physics*, 21, 16319–16347, <https://doi.org/10.5194/acp-21-16319-2021>, 2021.

873 874 875

876 877

878 Dansgaard, W.: Stable isotopes in precipitation., *Tellus*, 16, 436–468, 1964.

879 880 881

882 Dumarey, R., Temmerman, E., Adams, R., and Hoste, J.: The accuracy of the vapour-injection calibration method for the determination of mercury by amalgamation/cold-vapour atomic absorption spectrometry, *Analytica Chimica Acta*, 170, 337–340, 1985.

883 884 885

886 Durack, P. J., Taylor, K. E., Ames, S., Po-Chedley, S., and Mauzey, C.: PCMDI AMIP SST and sea-ice boundary conditions version 1.1.8, , <https://doi.org/10.22033/ESGF/input4MIPs.16921>, 2022.

887 Dütsch, M., Pfahl, S., and Wernli, H.: Drivers of $\delta^{2\text{H}}$ variations in an idealized extratropical cyclone, *Geophysical Research Letters*, 43, 5401–5408, 2016.

886 Edwards, B. A., Kushner, D. S., Outridge, P. M., Wang, F. (2021). Fifty years of volcanic mercury
887 emission research: Knowledge gaps and future directions. *Science of The Total Environment*, 757,
888 143800. <https://doi.org/10.1016/j.scitotenv.2020.143800>.

889

890 El Yazidi, A., Ramonet, M., Ciais, P., Broquet, G., Pison, I., Abbaris, A., Brunner, D., Conil, S.,
891 Delmotte, M., Gheusi, F., and others: Identification of spikes associated with local sources in
892 continuous time series of atmospheric CO, CO₂ and CH₄, *Atmospheric Measurement Techniques*, 11,
893 1599–1614, 2018.

894 Eyring, V., Bony, S., Meehl, G. A., Senior, C. A., Stevens, B., Stouffer, R. J., and Taylor, K. E.:
895 Overview of the Coupled Model Intercomparison Project Phase 6 (CMIP6) experimental design and
896 organization, *Geoscientific Model Development*, 9, 1937–1958, <https://doi.org/10.5194/gmd-9-1937-2016>, 2016.

897

898 Fain, X.; Obrist, D.; Hallar, A. G.; Mccubbin, I.; Rahn, T. High levels of reactive gaseous mercury
899 observed at a high elevation research laboratory in the Rocky Mountains *Atmos. Chem. Phys.* 2009, 9 (20) 8049– 8060 DOI: 10.5194/acp-9-8049-2009.

900

901

902 Fitzgerald, W. F. and Gill, G. A.: Subnanogram determination of mercury by two-stage gold
903 amalgamation and gas phase detection applied to atmospheric analysis, *Analytical chemistry*, 51,
904 1714–1720, 1979.

905 Fogt, R. and Marshall, G.: The Southern Annular Mode: Variability, trends, and climate impacts
906 across the Southern Hemisphere, *Wiley Interdisciplinary Reviews: Climate Change*, 11,
907 <https://doi.org/10.1002/wcc.652>, 2020.

908

909

910 Fu, X., Maruszczak, N., Wang, X., Gheusi, F. and Sonke, J.: The isotopic composition of gaseous
911 elemental mercury in the free troposphere of the Pic du Midi Observatory, France. *Environmental
912 Science & Technology*. 50. 10.1021/acs.est.6b00033, 2016

913

914 Galewsky, J., Steen-Larsen, H. C., Field, R. D., Worden, J., Risi, C., and Schneider, M.: Stable
915 isotopes in atmospheric water vapor and applications to the hydrologic cycle, *Reviews of Geophysics*,
916 54, 809–865, 2016.

917

918 Gaudry, A., Ascencio, J., and Lambert, G.: Preliminary study of CO₂ variations at Amsterdam Island
919 (Territoire des Terres Australes et Antarctiques Francaises), *Journal of Geophysical Research: Oceans*,
920 88, 1323–1329, 1983.

921

922 Graf, P., Wernli, H., Pfahl, S., and Sodemann, H.: A new interpretative framework for below-cloud
923 effects on stable water isotopes in vapour and rain, *Atmospheric Chemistry and Physics*, 19, 747–765,
924 2019.

925

926 Gros, V., Poisson, N., Martin, D., Kanakidou, M., and Bonsang, B.: Observations and modeling of the
927 seasonal variation of surface ozone at Amsterdam Island: 1994–1996, *Journal of Geophysical
928 Research: Atmospheres*, 103, 28103–28109, 1998.

929

930 Gros, V., Bonsang, B., Martin, D., Novelli, P., and Kazan, V.: Carbon monoxide short term
931 measurements at Amsterdam island: estimations of biomass burning emission rates, *Chemosphere-
932 Global Change Science*, 1, 163–172, 1999.

933

934 Gaffney J, Marley N. In-depth review of atmospheric mercury: sources, transformations, and potential
935 sinks. *Energy and Emission Control Technologies*. 2014;2:1-21 <https://doi.org/10.2147/EECT.S37038>.

936

937 Guilpart, E., Vimeux, F., Evan, S., Brioude, J., Metzger, J., Barthe, C., Risi, C., and Cattani, O.: The
938 isotopic composition of near-surface water vapor at the Maïdo observatory (Reunion Island,

939

932 southwestern Indian Ocean) documents the controls of the humidity of the subtropical troposphere,
933 Journal of Geophysical Research: Atmospheres, 122, 9628–9650,
934 <https://doi.org/10.1002/2017JD026791>, 2017.

935

936 Gustin, M. S., Amos, H. M., Huang, J., Miller, M. B., and Heidecorn, K.: Measuring and modeling
937 mercury in the atmosphere: a critical review, *Atmos. Chem. Phys.*, 15, 5697–5713,
938 <https://doi.org/10.5194/acp-15-5697-2015>, 2015.

939

940 Gustin, M. S., Bank, M. S., Bishop, K., Bowman, K., Brafireun, B., Chételat, J., Eckley, C. S.,
941 Hammerschmidt, C. R., Lamborg, C., Lyman, S., Martínez-Cortizas, A., Sommar, J., Tsz-Ki Tsui, M.,
942 & Zhang, T. (2020). Mercury biogeochemical cycling: A synthesis of recent scientific advances. *Science*
943 of the Total Environment

944 737, 139619. <https://doi.org/10.1016/j.scitotenv.2020.139619>.

945 Gworek, B., Dmuchowski, W. & Baczecka-Dąbrowska, A.H. Mercury in the terrestrial environment:
946 a review. *Environ Sci Eur* 32, 128 (2020). <https://doi.org/10.1186/s12302-020-00401-x>.

947

948 Henze, D., Noone, D., and Toohey, D.: Aircraft measurements of water vapor heavy isotope ratios in
949 the marine boundary layer and lower troposphere during ORACLES, *Earth Syst. Sci. Data*, 14, 1811–
950 1829, <https://doi.org/10.5194/essd-14-1811-2022>, 2022.

951

952 Hersbach, H., Bell, B., Berrisford, P., Hirahara, S., Horányi, A., Muñoz-Sabater, J., Nicolas, J.,
953 Peubey, C., Radu, R., Schepers, D., Simmons, A., Soci, C., Abdalla, S., Abellán, X., Balsamo, G.,
954 Bechtold, P., Biavati, G., Bidlot, J., Bonavita, M., De Chiara, G., Dahlgren, P., Dee, D., Diamantakis,
955 M., Dragani, R., Flemming, J., Forbes, R., Fuentes, M., Geer, A., Haimberger, L., Healy, S., Hogan,
956 R. J., Hólm, E., Janisková, M., Keeley, S., Laloyaux, P., Lopez, P., Lupu, C., Radnoti, G., de Rosnay,
957 P., Rozum, I., Vamborg, F., Villaume, S., and Thépaut, J.-N.: The ERA5 global reanalysis, *Quarterly*
958 *Journal of the Royal Meteorological Society*, 146, 1999–2049, <https://doi.org/10.1002/qj.3803>, 2020.

959 Hoang, C., Magand, O., Brioude, J., Dimuro, A., Brunet, C., Ah-Peng, C., Bertrand, Y., Dommergue,
960 A., Lei, Y. D., and Wania, F.: Probing the limits of sampling gaseous elemental mercury passively in
961 the remote atmosphere, *Environ. Sci.: Atmos.*, 3, 268–281, <https://doi.org/10.1039/D2EA00119E>,
962 2023.

963 Hourdin, F., Rio, C., Grandpeix, J.-Y., Madeleine, J.-B., Cheruy, F., Rochetin, N., Jam, A., Musat, I.,
964 Idelkadi, A., Fairhead, L., Foujols, M.-A., Mellul, L., Traore, A.-K., Dufresne, J.-L., Boucher, O.,
965 Lefebvre, M.-P., Millour, E., Vignon, E., Jouhaud, J., Diallo, F. B., Lott, F., Gastineau, G., Caubel, A.,
966 Meurdesoif, Y., and Ghattas, J.: LMDZ6A: The Atmospheric Component of the IPSL Climate Model
967 With Improved and Better Tuned Physics, *Journal of Advances in Modeling Earth Systems*, 12,
968 e2019MS001892, <https://doi.org/10.1029/2019MS001892>, 2020.

969 Jiskra, M., Sonke, J. E., Obrist, D., Bieser, J., Ebinghaus, R., Myhre, C. L., Pfaffhuber, K. A.,
970 Wängberg, I., Kyllonen, K., Worthy, D., Martin, L. G., Labuschagne, C., Mkololo, T., Ramonet, M.,
971 Magand, O., and Dommergue, A.: A vegetation control on seasonal variations in global atmospheric
972 mercury concentrations, *Nature Geoscience*, 11, 244–250, <https://doi.org/10.1038/s41561-018-0078-8>,
973 2018.

974 Jullien, N., Vignon, É., Sprenger, M., Aemisegger, F., and Berne, A.: Synoptic conditions and
975 atmospheric moisture pathways associated with virga and precipitation over coastal Adélie Land in
976 Antarctica, *The Cryosphere*, 14, 1685–1702, <https://doi.org/10.5194/tc-14-1685-2020>, 2020.

977 Koenig, A.M., Magand, O., Verreyken, B., Brioude, J., Amelynck, C., Schoon, N., Colomb, A.,
978 Ramonet, M., Sha, M.K., Cammas, J.P., Sonke, J.E., Dommergue, A., 2023. Mercury in the free
979 troposphere and bidirectional atmosphere-vegetation exchanges – Insights from Maito observatory in
980 the southern hemisphere tropics. *Atmos. Chem. Phys.*, 23, 1309–1328, <https://doi.org/10.5194/acp-23-1309-2023>

981

982

983 Lee, K.-O., Aemisegger, F., Pfahl, S., Flamant, C., Lacour, J.-L., and Chaboureau, J.-P.: Contrasting
984 stable water isotope signals from convective and large-scale precipitation phases of a heavy
985 precipitation event in southern Italy during HyMeX IOP 13: a modelling perspective, *Atmospheric*
986 *Chemistry and Physics*, 19, 7487–7506, 2019.

987 LeGrande, A. N. and Schmidt, G. A.: Global gridded data set of the oxygen isotopic composition in
988 seawater, *Geophysical Research Letters*, 33, 1–5, <https://doi.org/10.1029/2006GL026011>, 2006.

989 Leroy-Dos Santos, C., Masson-Delmotte, V., Casado, M., Fourré, E., Steen-Larsen, H. C., Maturilli,
990 M., Orsi, A., Berchet, A., Cattani, O., Minster, B., Gherardi, J., and Landais, A.: A 4.5 Year-Long
991 Record of Svalbard Water Vapor Isotopic Composition Documents Winter Air Mass Origin, *Journal*
992 *of Geophysical Research: Atmospheres*, 125, e2020JD032681–e2020JD032681,
993 <https://doi.org/10.1029/2020JD032681>, 2020.

994 Leroy-Dos Santos, C., Casado, M., Prié, F., Jossoud, O., Kerstel, E., Farradèche, M., Kassi, S., Fourré,
995 E., and Landais, A.: A dedicated robust instrument for water vapor generation at low humidity for use
996 with a laser water isotope analyzer in cold and dry polar regions, *Atmospheric Measurement*
997 *Techniques*, 14, 2907–2918, <https://doi.org/10.5194/amt-14-2907-2021>, 2021.

998 Li, C., Enrico, M., Magand, O., Araujo, B. F., Le Roux, G., Osterwalder, S., Dommergue, A.,
999 Bertrand, Y., Brioude, J., De Vleeschouwer, F., and others: A peat core Hg stable isotope
1000 reconstruction of Holocene atmospheric Hg deposition at Amsterdam Island (37.8 °S), *Geochimica et*
1001 *Cosmochimica Acta*, 341, 62–74, 2023.

1002 Lindberg, S., Bullock, R., Ebinghaus, R., Engstrom, D., Feng, X., Fitzgerald, W., Pirrone, N., Prestbo,
1003 E., and Seigneur, C.: A synthesis of progress and uncertainties in attributing the sources of mercury in
1004 deposition., *Ambio*, 36, 19–32, 2007, [https://doi.org/10.1579/0044-7447\(2007\)1002-19](https://doi.org/10.1579/0044-7447(2007)1002-19)

1005 Lyman, S. N.; Jaffe, D. A. Formation and fate of oxidized mercury in the upper troposphere and lower
1006 stratosphere *Nat. Geosci.* 2012, 5 (2) 114– 117 doi: 10.1038/ngeo1353

1007

1008 Magand, O. and Dommergue, A.: Continuous measurements of atmospheric mercury at Maito
1009 Observatory (L2), Global Mercury Observation System [data set], 2022.

1010 Munksgaard, N. C., Zwart, C., Kurita, N., Bass, A., Nott, J., and Bird, M. I.: Stable isotope anatomy of
1011 tropical cyclone Ita, north-eastern Australia, April 2014, *PLoS one*, 10, e0119728, 2015.

1012 Murphy, D. M.; Hudson, P. K.; Thomson, D. S.; Sheridan, P. J.; Wilson, J. C. Observations of Mercury-
1013 Containing Aerosols. *Environ. Sci. Technol.* 2006, 40 (10), 3163–3167.

1014

1015 Noone, D.: Pairing Measurements of the Water Vapor Isotope Ratio with Humidity to Deduce
1016 Atmospheric Moistening and Dehydration in the Tropical Midtroposphere, *Journal of Climate*, 25,
1017 4476–4494, <https://doi.org/10.1175/JCLI-D-11-00582.1>, 2012.

1018 Pisso, I., Sollum, E., Grythe, H., Kristiansen, N. I., Cassiani, M., Eckhardt, S., Arnold, D., Morton, D.,
1019 Thompson, R. L., Groot Zwaftink, C. D., Evangelou, N., Sodemann, H., Haimberger, L., Henne, S.,
1020 Brunner, D., Burkhardt, J. F., Fouilloux, A., Brioude, J., Philipp, A., Seibert, P., and Stohl, A.: The
1021 Lagrangian particle dispersion model FLEXPART version 10.4, *Geoscientific Model Development*,
1022 12, 4955–4997, <https://doi.org/10.5194/gmd-12-4955-2019>, 2019.

1023 Polian, G., Lambert, G., Ardouin, B., and Jegou, A.: Long-range transport of continental radon in
1024 subantarctic and antarctic areas, *Tellus B: Chemical and Physical Meteorology*, 38, 178–189, 1986.

1025 Risi, C., Bony, S., Vimeux, F., and Jouzel, J.: Water-stable isotopes in the LMDZ4 general circulation
1026 model: Model evaluation for present-day and past climates and applications to climatic interpretations

1027 of tropical isotopic records, *Journal of Geophysical Research Atmospheres*, 115,
1028 <https://doi.org/10.1029/2009JD013255>, 2010.

1029 Ryan, B.F., J.J. Katzfey, D.J. Abbs, C. Jakob, U. Lohmann, B. Rockel, L.D. Rotstayn, R.E. Stewart,
1030 K.K. Szeto, G. Tselioudis, and M.K. Yau, 2000: Simulations of a cold front by cloud-resolving,
1031 limited-area, and large-scale models, and a model evaluation using in situ and satellite observations.
1032 *Mon. Weather Rev.*, **128**, 3218–3235, doi:10.1175/1520-0493(2000)

1033

1034 Sciare, J., Mihalopoulos, N., and Dentener, F.: Interannual variability of atmospheric dimethylsulfide
1035 in the southern Indian Ocean, *Journal of Geophysical Research: Atmospheres*, 105, 26369–26377,
1036 2000.

1037 Sciare, J., Favez, O., Sarda-Estève, R., Oikonomou, K., Cachier, H., and Kazan, V.: Long-term
1038 observations of carbonaceous aerosols in the Austral Ocean atmosphere: Evidence of a biogenic
1039 marine organic source, *Journal of Geophysical Research: Atmospheres*, 114, 2009.

1040 Shah, V., Jacob, D. J., Thackray, C. P., Wang, X., Sunderland, E. M., Dibble, T. S., Saiz-Lopez, A., C̄
1041 ernušák, I., Kellö, V., astro, P. J., Wu, R., and Wang, C.: Improved Mechanistic Model of the
1042 Atmospheric Redox Chemistry of Mercury, *Environ. Sci. Technol.*, 55, 14445–14456,
1043 <https://doi.org/10.1021/acs.est.1c03160>, 2021.

1044

1045 Sheu, G. R.; Lin, N. H.; Wang, J. L.; Lee, C. T.; Yang, C. F. O.; Wang, S. H. Temporal distribution and
1046 potential sources of atmospheric mercury measured at a high-elevation background station in
1047 Taiwan *Atmos. Environ.* 2010, 44 (20) 2393– 2400 DOI: 10.1016/j.atmosenv.2010.04.009

1048

1049 Sherwood, S. C., Bony, S., and Dufresne, J.-L.: Spread in model climate sensitivity traced to
1050 atmospheric convective mixing, *Nature*, 505, 37–42, <https://doi.org/10.1038/nature12829>, 2014.

1051 Sillman, S., Marsik, F. J., Al-Wali, K. I., Keeler, G. J., and Landis, M. S.: Reactive mercury in the
1052 troposphere: Model formation and results for Florida, the northeastern United States, and the Atlantic
1053 Ocean, *Journal of Geophysical Research: Atmospheres*, 112, 2007.

1054 Slemr, F., Angot, H., Dommergue, A., Magand, O., Barret, M., Weigelt, A., Ebinghaus, R., Brunke,
1055 E.-G., Pfaffhuber, K. A., Edwards, G., and others: Comparison of mercury concentrations measured at
1056 several sites in the Southern Hemisphere, *Atmospheric Chemistry and Physics*, 15, 3125–3133, 2015.

1057 Slemr, F., Martin, L., Labuschagne, C., Mkololo, T., Angot, H., Magand, O., Dommergue, A., Garat,
1058 P., Ramonet, M., and Bieser, J.: Atmospheric mercury in the Southern Hemisphere—Part 1: Trend and
1059 inter-annual variations in atmospheric mercury at Cape Point, South Africa, in 2007–2017, and on
1060 Amsterdam Island in 2012–2017, *Atmospheric Chemistry and Physics*, 20, 7683–7692, 2020.

1061 Sprovieri, F., Pirrone, N., Bencardino, M., D'amore, F., Carbone, F., Cinnirella, S., Mannarino, V.,
1062 Landis, M., Ebinghaus, R., Weigelt, A., and others: Atmospheric mercury concentrations observed at
1063 ground-based monitoring sites globally distributed in the framework of the GMOS network,
1064 *Atmospheric chemistry and physics*, 16, 11915–11935, 2016.

1065 Steen-Larsen, H. C., Johnsen, S. J., Masson-Delmotte, V., Stenni, B., Risi, C., Sodemann, H., Balslev-
1066 Clausen, D., Blunier, T., Dahl-Jensen, D., Elleh??j, M. D., Falourd, S., Grindsted, A., Gkinis, V.,
1067 Jouzel, J., Popp, T., Sheldon, S., Simonsen, S. B., Sjolte, J., Steffensen, J. P., Sperlich, P.,
1068 Sveinbj??rnsd??ttir, A. E., Vinther, B. M., and White, J. W. C.: Continuous monitoring of summer
1069 surface water vapor isotopic composition above the Greenland Ice Sheet, *Atmospheric Chemistry and*
1070 *Physics*, 13, 4815–4828, <https://doi.org/10.5194/acp-13-4815-2013>, 2013.

1071 Steffen, A., Scherz, T., Olson, M., Gay, D., and Blanchard, P.: A comparison of data quality control
1072 protocols for atmospheric mercury speciation measurements, *Journal of Environmental Monitoring*,
1073 14, 752–765, 2012.

1074 Stevens, B., Giorgetta, M., Esch, M., Mauritsen, T., Crueger, T., Rast, S., Salzmann, M., Schmidt, H.,
1075 Bader, J., Block, K., Brokopf, R., Fast, I., Kinne, S., Kornblueh, L., Lohmann, U., Pincus, R.,
1076 Reichler, T., and Roeckner, E.: Atmospheric component of the MPI-M Earth System Model:
1077 ECHAM6, *Journal of Advances in Modeling Earth Systems*, 5, 146–172,
1078 <https://doi.org/10.1002/jame.20015>, 2013.

1079 Swartzendruber, P., Chand, D., Jaffe, D., Smith, J., Reidmiller, D., Gratz, L., Keeler, J., Strode, S.,
1080 Jaeglé, L., and Talbot, R.: Vertical distribution of mercury, CO, ozone, and aerosol scattering
1081 coefficient in the Pacific Northwest during the spring 2006 INTEX-B campaign, *Journal of*
1082 *Geophysical Research: Atmospheres*, 113, 2008.

1083 Swartzendruber, P. C., Jaffe, D. A., Prestbo, E., Weiss-Penzias, P., Selin, N. E., Park, R., Jacob, D. J.,
1084 Strode, S., and Jaegle, L.: Observations of reactive gaseous mercury in the free troposphere at the
1085 Mount Bachelor Observatory, *Journal of Geophysical Research: Atmospheres*, 111, 2006.

1086 Swartzendruber, P.; Chand, D.; Jaffe, D. A.; Smith, J.; Reidmiller, D.; Gratz, L.; Keeler, J.; Strode, S.;
1087 Jaegle, L.; Talbot, R. Vertical distribution of mercury, CO, ozone, and aerosol scattering coefficient in
1088 the Pacific Northwest during the spring 2006 INTEX-B campaign. *J. Geophys. Res., [Atmos.]* 2008,
1089 113, D10305.

1090 Talbot, R., Mao, H., Scheuer, E., Dibb, J., and Avery, M.: Total depletion of Hg in the upper
1091 troposphere–lower stratosphere, *Geophysical Research Letters*, 34, 2007.

1092 Talbot, R., Mao, H., Scheuer, E., Dibb, J., Avery, M., Browell, E., Sachse, G., Vay, S., Blake, D.,
1093 Huey, G., and others: Factors influencing the large-scale distribution of Hg° in the Mexico City area
1094 and over the North Pacific, *Atmospheric Chemistry and Physics*, 8, 2103–2114, 2008.

1095 Taylor, K. E., Williamson, D., and Zwiers, F.: The sea surface temperature and sea ice concentration
1096 boundary conditions for AMIP II simulations”, PCMDI Report 60, Program for Climate Model
1097 Diagnosis and Intercomparison, Lawrence Livermore National Laboratory, 2000.

1098 Thurnherr, I., Kozachek, A., Graf, P., Weng, Y., Bolshiyanov, D., Landwehr, S., Pfahl, S., Schmale,
1099 J., Sodemann, H., Steen-Larsen, H. C., and others: Meridional and vertical variations of the water
1100 vapour isotopic composition in the marine boundary layer over the Atlantic and Southern Ocean,
1101 *Atmospheric Chemistry and Physics*, 20, 5811–5835, 2020.

1102 Tremoy, G., Vimeux, F., Cattani, O., Mayaki, S., Souley, I., and Favreau, G.: Measurements of water
1103 vapor isotope ratios with wavelength-scanned cavity ring-down spectroscopy technology: New
1104 insights and important caveats for deuterium excess measurements in tropical areas in comparison
1105 with isotope-ratio mass spectrometry, *Rapid Communications in Mass Spectrometry*, 25, 3469–3480,
1106 <https://doi.org/10.1002/rcm.5252>, 2011.

1107 Tremoy, G., Vimeux, F., Mayaki, S., Souley, I., Cattani, O., Risi, C., Favreau, G., and Oi, M.: A 1-
1108 year long $\delta^{18}\text{O}$ record of water vapor in Niamey (Niger) reveals insightful atmospheric processes at
1109 different timescales, *Geophysical Research Letters*, 39, 2012.

1110 Tremoy, G., Vimeux, F., Soumana, S., Souley, I., Risi, C., Favreau, G., and Oi, M.: Clustering
1111 mesoscale convective systems with laser-based water vapor $\delta^{18}\text{O}$ monitoring in Niamey (Niger),
1112 *Journal of Geophysical Research: Atmospheres*, 119, 5079–5103,
1113 <https://doi.org/10.1002/2013JD020968>, 2014.

1115 Wang, H., Fyke, J. G., Lenaerts, J. T. M., Nusbaumer, J. M., Singh, H., Noone, D., Rasch, P. J., and
1116 Zhang, R.: Influence of sea-ice anomalies on Antarctic precipitation using source attribution in the
1117 Community Earth System Model, *The Cryosphere*, 14, 429–444, <https://doi.org/10.5194/tc-14-429-2020>, 2020.

1119

1120 Weiss-Penzias, P.; Gustin, M. S.; Lyman, S. N. Observations of speciated atmospheric mercury at three
1121 sites in Nevada: Evidence for a free tropospheric source of reactive gaseous mercury. *J. Geophys. Res.*
1122 [Atmos.] 2009, 114, D14302.

1123

1124 Weng, Y., Touzeau, A., and Sodemann, H.: Correcting the impact of the isotope composition on the
1125 mixing ratio dependency of water vapour isotope measurements with cavity ring-down spectrometers,
1126 *Atmospheric Measurement Techniques*, 13, 3167–3190, <https://doi.org/10.5194/amt-13-3167-2020>,
1127 2020.

1128 Worden, J., Noone, D., and Bowman, K.: Importance of rain evaporation and continental convection
1129 in the tropical water cycle., *Nature*, 445, 528–532, <https://doi.org/10.1038/nature05508>, 2007.

1130

1131

